**RESEARCH ARTICLE**

ADVANCED MATERIALS
www.advmat.de

# Stepwise Stiffening/Softening of and Cell Recovery from Reversibly Formulated Hydrogel Interpenetrating Networks

*Irina Kopyeva, Ethan C. Goldner, Jack W. Hoye, Shiyu Yang, Mary C. Regier, John C. Bradford, Kaitlyn R. Vera, Ross C. Bretherton, Jennifer L. Robinson, and Cole A. DeForest**

**Biomechanical contributions of the extracellular matrix underpin cell growth and proliferation, differentiation, signal transduction, and other fate decisions. As such, biomaterials whose mechanics can be spatiotemporally altered-particularly in a reversible manner- are extremely valuable for studying these mechanobiological phenomena. Herein, a poly(ethylene glycol) (PEG)-based hydrogel model consisting of two interpenetrating step-growth networks is introduced that are independently formed via largely orthogonal bioorthogonal chemistries and sequentially degraded with distinct recombinant sortases, affording reversibly tunable stiffness ranges that span healthy and diseased soft tissues (e.g., 500 Pa–6 kPa) alongside terminal cell recovery for pooled and/or single-cell analysis in a near "biologically invisible" manner. Spatiotemporal control of gelation within the primary supporting network is achieved via mask-based and two-photon lithography; these stiffened patterned regions can be subsequently returned to the original soft state following sortase-based secondary network degradation. Using this approach, the effects of 4D-triggered network mechanical changes on human mesenchymal stem cell morphology and Hippo signaling, as well as Caco-2 colorectal cancer cell mechanomemory using transcriptomics and metabolic assays are investigated. This platform is expected to be of broad utility for studying and directing mechanobiological phenomena, patterned cell fate, and disease resolution in softer matrices.**

## 1. Introduction

The interactions between cells and their environment are complex and dynamic. During development and disease, the extracellular matrix (ECM) undergoes major remodeling, resulting in changes in biochemical composition, biomechanical properties, and topography.[1–3] ECM biomechanics are known to play a crucial role in cell growth, differentiation, proliferation, and signal transduction.[4] The elastic modulus ($E$), or the stiffness, varies greatly among different tissues, ranging from 17 Pa (fat) to 20 GPa (cortical bone), supporting their diverging form and function.[5] Cells translate mechanical stimuli in numerous ways; among the most studied mechanosensory complexes are focal adhesions, which initiate a complex signaling cascade when subjected to external force.[4] Downstream, transcription factors such as Yes-associated protein (YAP) and the transcriptional coactivator with PDZ-binding motif (TAZ) transmit cytoskeletal tension to the nucleus, impacting gene

---

I. Kopyeva, J. C. Bradford, R. C. Bretherton, C. A. DeForest
Department of Bioengineering
University of Washington
Seattle, WA 98105, USA
E-mail: profcole@uw.edu

E. C. Goldner, J. W. Hoye, S. Yang, K. R. Vera, C. A. DeForest
Department of Chemical Engineering
University of Washington
Seattle, WA 98105, USA

M. C. Regier, J. C. Bradford, R. C. Bretherton, J. L. Robinson, C. A. DeForest
Institute of Stem Cell & Regenerative Medicine
University of Washington
Seattle, WA 98105, USA

J. L. Robinson
Department of Orthopedic Surgery and Sports Medicine
University of Washington
Seattle, WA 98105, USA

J. L. Robinson
Department of Mechanical Engineering
University of Washington
Seattle, WA 98105, USA

J. L. Robinson, C. A. DeForest
Molecular Engineering & Sciences Institute
University of Washington
Seattle, WA 98105, USA

C. A. DeForest
Department of Chemistry
University of Washington
Seattle, WA 98105, USA

C. A. DeForest
Institute for Protein Design
University of Washington
Seattle, WA 98105, USA

The ORCID identification number(s) for the author(s) of this article can be found under https://doi.org/10.1002/adma.202404880

**DOI: 10.1002/adma.202404880**

expression.[6–8] Numerous diseases can be viewed in terms of mechanical dysregulation of tissue—two common examples being fibrosis and cancer. In fibrosis, fibroblasts respond to increased ECM stiffness and activate, secreting excess ECM proteins, which in turn further stiffens the matrix and perpetuates a self-amplifying feedback loop.[9] In breast cancer and other solid tumors, stiffening (from 150 Pa to upward of 6 kPa) of the matrix drives malignancy.[10,11]

Synthetic hydrogels with viscoelastic and tunable properties akin to tissue offer an attractive platform for studying mechanotransduction phenomena. Specifically, materials that can change their properties in situ afford researchers the ability to simulate the dynamic nature of the ECM.[12] Stiffening hydrogels can be used to initiate pro-fibrotic signaling and mesenchymal and muscle stem cell differentiation, and to study these events in vitro.[13–15] Yet, these systems cannot resolve the cellular response to softening events, such as during cervical remodeling during pregnancy,[16] or address whether pathologies, such as cancer progression, could be reversed by modulating ECM mechanics.[17,18] While photodegradable hydrogels have been developed for triggered material softening and reversible modulation of mechanics,[19–23] these systems exhibit high light absorptivity/attenuation that confines softening to the surface; dynamic softening studies are thus limited to 2D-seeded cells. Other systems based on stimuli-responsive protein cross–linkers have achieved reversible modulation of bulk mechanics, but do so with a limited dynamic range[24] or have relied on chemistries that were not shown to be compatible with 3D cell encapsulation protocols.[25,26] Finally, methods such as reversibly DNA-crosslinked hydrogels, other cation-induced physical cross–linking systems, or magnetic hydrogels offer excellent bulk modulation of mechanics, but limited spatial control.[27–31] To improve upon these models, we designed a dynamic hydrogel culture system in which mechanics could be reversibly patterned across a wide range of bulk stiffnesses and would allow for encapsulated cells to be subsequently recovered in a "biologically invisible" manner for downstream pooled and/or single-cell-based analysis.

To address our design criteria, we selected *S. aureus* transpeptidase, Sortase A (SrtA), as a bioorthogonal enzyme for hydrogel degradation. Wild-type SrtA binds to the sorting motif "LPXTG" (where X is any amino acid) and cleaves between the Thr-Gly peptide bond. The Thr reacts with a Gly-Gly-Gly motif to form an LPXTGGG product, simultaneously displacing any sequence C-terminal to the sorting motif's Thr. This sorting motif is extremely uncommon in the mammalian proteome, rendering this reaction largely bioorthogonal.[32] SrtA has been utilized to rapidly release cells from hydrogels for downstream processing, as well as for modulating hydrogel mechanics, with no deleterious effects on survival and signaling.[32–34] Wild-type SrtA has evolved to yield two orthogonal sortases—eSrtA(2A9) and eSrtA(4S9) (respectively denoted 2A9 and 4S9)–that recognize with high specificity the sequences LAETG and LPESG, respectively.[35] Previously, we have demonstrated that these peptide sequences can be included within single-network hydrogel cross–linkers to selectively release cells from materials in a "biologically invisible" manner, with minimal perturbation of the transcriptome of sensitive primary cell types; this method allowed for the construction of complex, multimaterial, 3D cell culture models using open-microfluidic patterning.[33] Building on these efforts, we envisioned creating a hydrogel made up of interpenetrating networks (IPNs), in which each interpenetrating single network could be independently formed and degraded to permit step-wise stiffening, softening, and cell recovery via full network degradation (**Figure** 1a,b).

Our IPN unites two popular bioorthogonal reactions used for step-growth hydrogel biomaterial formation: a spontaneous strain-promoted azide-alkyne cycloaddition (SPAAC) between a terminal azide and a strained alkyne, and a thiol-ene photoreaction involving the radical-mediated addition of a thiol to a strained alkene (Figure 1c,d).[36,37] Poly(ethylene glycol) (PEG) star polymers were end-functionalized with either bicyclononyne (BCN) or norbornene (NB) moieties, which respectively react with diazide- or dicysteine-containing peptides - each degradable with an orthogonal sortase and the same cell-secreted matrix metalloproteases (MMPs) (i.e., both contain the same MMP-cleavable peptide sequence but a different sortase recognition motif) - to form interpenetrating covalent networks. Notably, since SPAAC and thiol-ene reactions are kinetically orthogonal,[38] IPNs can be formed in a single reaction mixture via "self-sorting".[39] Further, the biochemical properties of each individual network can be distinctly tuned through pendant peptide incorporation (e.g., the inclusion of an azide-modified RGDS peptide enables cell adhesivity to the SPAAC network, but not to the thiol-ene network), a useful feature for maintaining constant material biofunctionalization throughout dynamic material stiffening/softening. We anticipate this platform will prove uniquely powerful for studying mechanotransduction and memory in 4D.

## 2. Results

### 2.1. Interpenetrating Network mechanical properties are tunable

We first established that our baseline IPN could be formed in a one-pot, stepwise manner via photorheology. We allowed the primary SPAAC network to spontaneously form over the course of an hour and then illuminated the single-network hydrogel with near-UV light ($\lambda = 365$ nm, 10 mW cm$^{-2}$, 2 min) to form the interpenetrating secondary thiol-ene network. The storage modulus of the SPAAC network plateaued to 2241 ± 670 Pa at ≈1 h, and then sharply increased to 4848 ± 890 Pa upon photopolymerization of the thiol-ene secondary network (Figure 1e). Next, having established that our two-step method would yield the expected step up in shear storage modulus, we explored varying parameters to create IPN materials of various initial stiffnesses. Increasing the exposure time (0–2 min) led to significant increases in Young's moduli of swollen gels, as measured by atomic force microscopy (AFM) (Figure 1f); however, we observed a plateau after 1 min of exposure time, indicating complete thiol-ene polymerization within that time frame. Similarly, increasing the final concentration of the thiol-ene network in the gel formulation led to increases in swollen Young's moduli with the maximal 5 mM PEG-NB: 20 mM dicysteine condition achieving a modulus of 5687 ± 260 Pa (Figure 1g); however, these differences were not significant. Additionally, the inclusion of a pendant $N_3$-RGDS-$NH_2$ peptide, which was later used to facilitate cell adhesion to the matrix,[33] resulted in a small but expected decrease in Young's modulus (Figure S4, Supporting Information).

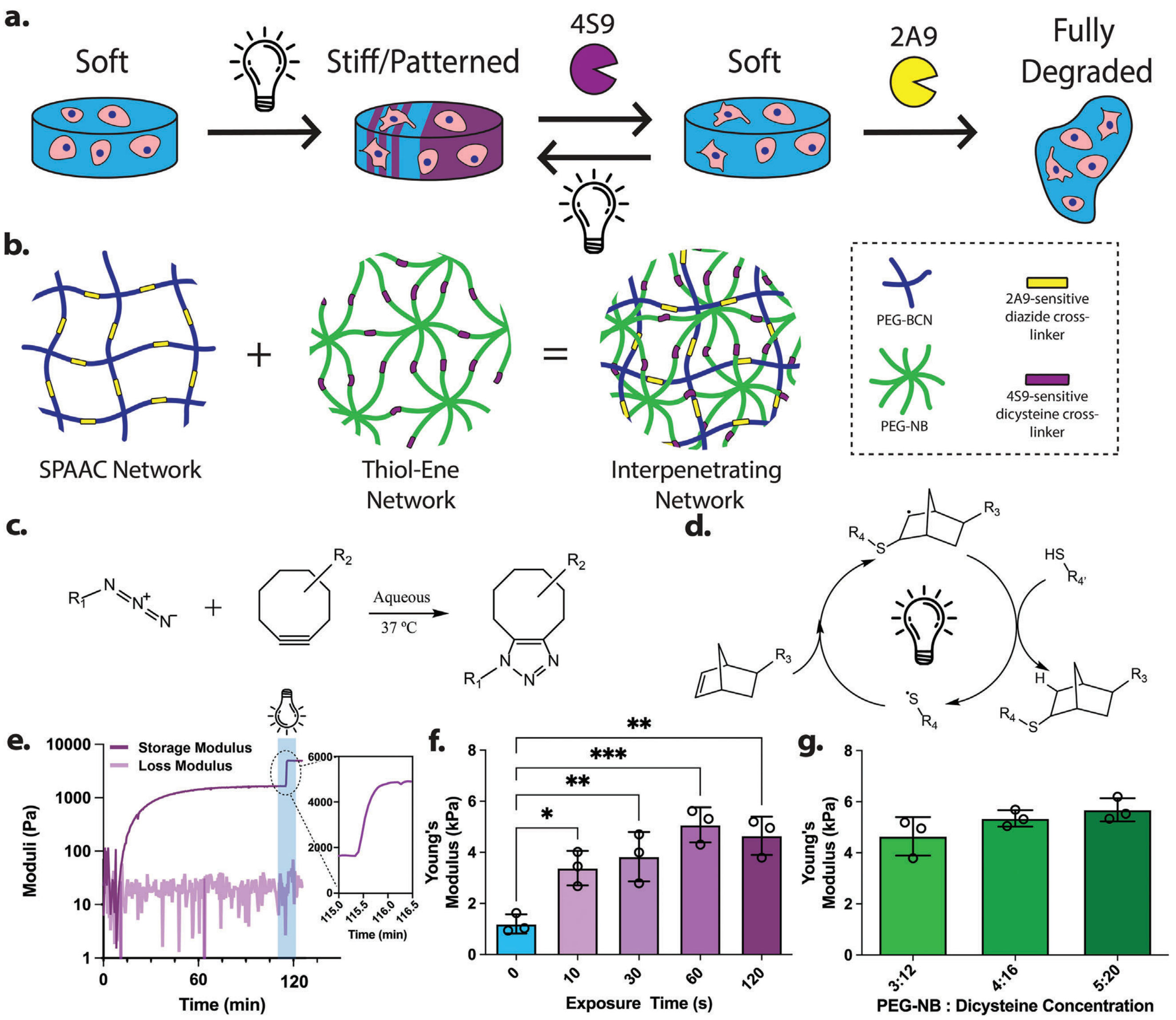

**Figure 1.** Interpenetrating networks are tunably formed. a) IPNs are reversibly formulated with spatiotemporal control using a collection of orthogonal network formation and degradation chemistries. b) IPNs are composed of two distinct PEG-based networks formed via two popular bioorthogonal reactions: c) strain-promoted azide-alkyne cycloaddition (SPAAC) and d) the radical-mediated and light-driven thiol-ene reaction. e) In situ photorheology demonstrates stepwise IPN formation; SPAAC network formation proceeds spontaneously in the presence of thiol-ene network precursors, the latter of which is rapidly photopolymerized. Inset shows a dramatic increase in storage modulus upon light exposure. f) Young's moduli as determined by AFM of swollen in PBS gels (initial concentrations 3 mM PEG-BCN: 6 mM diazide: 3 mM PEG-NB: 12 mM dicysteine: 1 mM LAP), post various light exposure times (0–2 min, 10 mW cm$^{-2}$). SPAAC gels—1196 ± 370 Pa; 10 s—3381 ± 670 Pa; 30 s—3829 ± 970 Pa; 1 min—5079 ± 690 Pa; 2 min—4648 ± 750 Pa. One-Way ANOVA, Tukey's post-hoc test. $^{*}p < 0.05$, $^{**}p < 0.01$, $^{***}p < 0.001$. g) Young's moduli as determined by AFM of swollen gels, keeping SPAAC network constant, but varying molarity of thiol-ene network. 3 mM PEG-NB—4648 ± 750 Pa; 4 mM PEG-NB—5352 ± 320 Pa; 5 mM PEG-NB—5687 ± 450 Pa.

### 2.2. Sortase treatments proceed orthogonally and yield a step down in Young's modulus

Our next goal was to demonstrate that our proposed method would allow for bulk hydrogel softening, achieved through conversion of our IPN gels to a single network through sortase-mediated degradation. While either network can be cross–linked with an either eSrtA-sensitive cross–link, for this initial study, we chose to include the 2A9-sensitive sequence "LAETG" on the diazide cross–linkers in the SPAAC network, and the 4S9-sensitive sequence "LPESG" on the dicysteine cross–linkers in the thiol-ene network (**Figure** 2a,b). Each peptide cross–linker also included the MMP-sensitive sequence "GPQGIWGQ" to allow for cell-mediated remodeling of the hydrogel matrix.[41,48]

While orthogonal sortase variants have been successfully deployed for degrading complex layered hydrogels,[33] this method has yet to be applied to selectively degrading interpenetrating networks, although other nonbioorthogonal enzymes

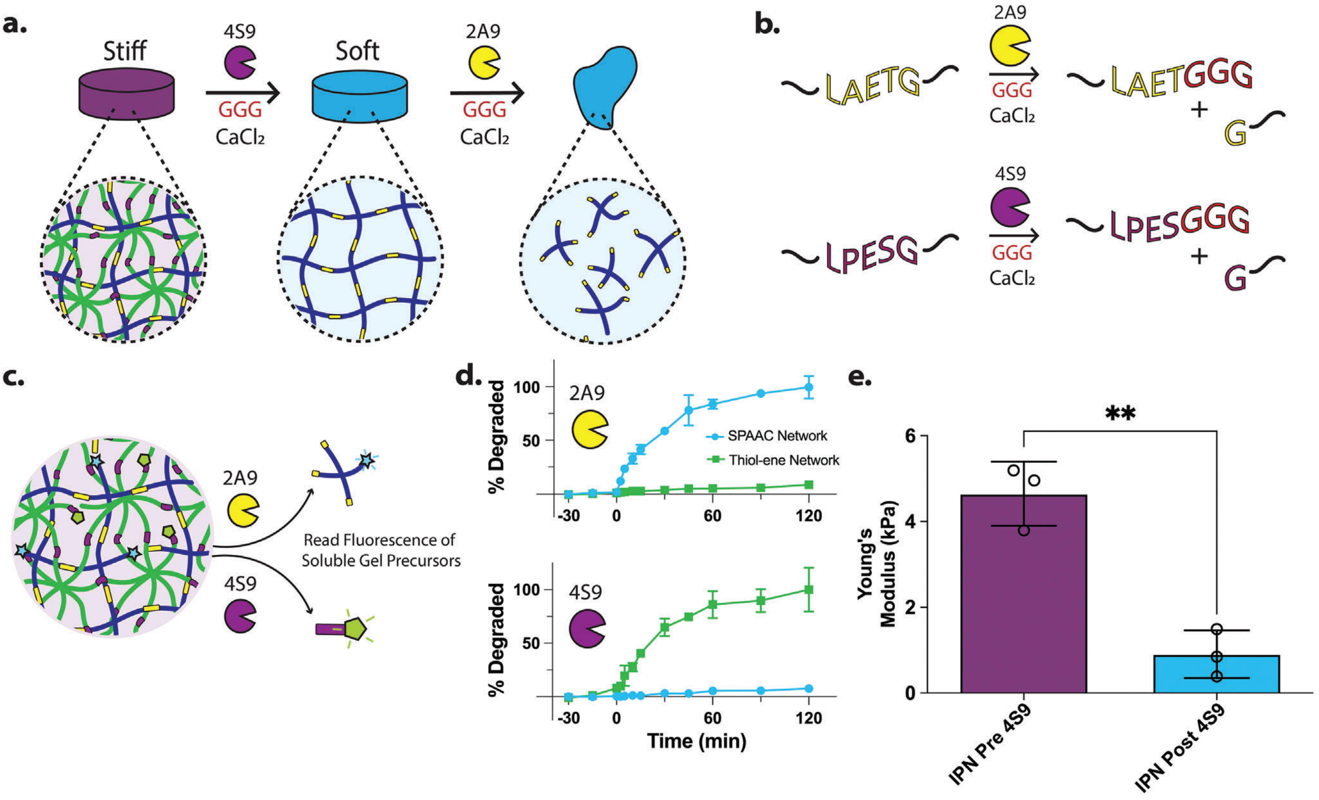

**Figure 2.** Interpenetrating networks can be independently degraded in a stepwise manner. a) IPNs are first treated with 4S9 to remove the thiol-ene network, and then fully degraded by treatment with 2A9 to yield fully soluble macromolecular building blocks. b) Peptide recognition sequences for 2A9 and 4S9 included in hydrogel cross–linkers and degradation reaction post-sortase treatment. c) Schematic depicting individual labeling of each network with distinct fluorophores, and the monomeric component released upon each sortase treatment, tracked by increases in supernatant fluorescence. d) Fluorophore release studies. At time = 0 min, 18 mM GGG, the respective sortase, and 1 mM CaCl$_2$ were added to the solution of the IPN hydrogels. Hydrogel degradation was tracked by monitoring supernatant fluorescence, with values normalized to those obtained from 100% degraded gels 12 h post-reaction. $N = 5$ gels per treatment. e) AFM measurements of IPN gels pre- and post-4S9 treatment. IPN pre-4S9 treatment: 4648 ± 750 Pa; IPN post-4S9 treatment: 908 ± 550 Pa. Unpaired t-test, $^{**}p = 0.0024$.

(e.g., alginate lyase, hyaluronidase, thrombin) have previously been employed.[6,49,50] In fact, to our knowledge, there are no prior reports of converting a fully synthetic polymer-based IPN to a single-network system using any stimulus. To monitor degradation via changes in supernatant fluorescence, we created IPNs whereby each network was sparsely tagged with a different fluorophore (Figure 2c), which upon cleavage and release, diffused into the supernatant. Whereas others have previously pre-incubated gels with sortase to allow for maximal diffusion and fast degradation kinetics,[32,33] given our ultimate need to conduct such degradation in the presence of cells, we chose to add both sortase and GGG simultaneously. Upon the addition of 50 µM 4S9 solution, 18 mM triglycine (GGG), and 10 mM CaCl$_2$ at t = 0, we observed rapid degradation. Treatment with 2A9 led to degradation of the SPAAC network, with very minimal perturbation of the thiol-ene network, as expected, and conversely, treatment with 4S9 led to degradation of the thiol-ene network, with minimal impact on SPAAC network integrity (Figure 2d). Following the end of the assay, the remaining gels were treated with the other sortase, resulting in a fully soluble mixture. Our results aligned with our previous findings, which demonstrated that 2A9 and 4S9 can degrade multimaterials in a fully orthogonal manner.[33] Intriguingly, degradation times for a 4-arm SPAAC network and an 8-arm thiol-ene network were almost identical: both reactions neared completion in 60 min. To maximize the mechanical difference between stiff and soft regimes, we chose to first treat our IPNs with 4S9 to degrade the 8-arm thiol-ene network (Figure 2a). AFM measurements pre- and post-4S9 treatment similarly demonstrated a significant drop in Young's modulus, with the softened modulus (878 ± 350 Pa) not statistically different from a single network SPAAC gel (1196 ± 210 Pa) (Figure 2e). The initial IPN moduli (4.6–5.7 kPa) presented match that of softer tissues, including that of diseased kidney glomeruli,[51] metastatic and primary colon cancer,[17,52] pancreatic ductal adenocarcinoma,[53] as well as other healthy examples.[54] Softened moduli, similarly, were in the range of healthy kidney, colon, and pancreatic tissue.[54]

### 2.3. Hydrogel formulations and 4S9 treatment are cytocompatible

After having established the ability to modulate bulk mechanics, we next assessed the suitability of this platform and method for 3D cell culture. 10T1/2 murine fibroblasts were encapsulated in SPAAC, thiol-ene, or IPN gels and cultured for 7 days. A subset of the IPNs were treated with 4S9 on day 3 of culture ("dy-

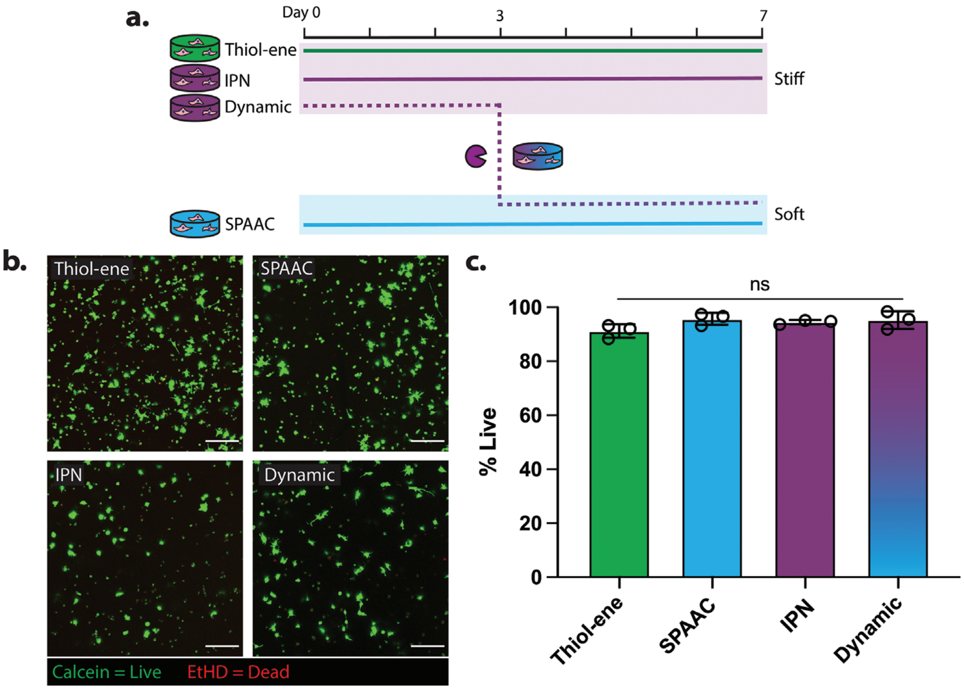

**Figure 3.** IPNs can be formed and dynamically softened in a cytocompatible manner. a) Experimental set-up for viability measurements. Static controls of thiol-ene, IPN, and SPAAC gels were compared against dynamic IPN gels treated with 4S9 on day 3 of culture. b) Maximum Image Projection (MIP) of representative images ($z = 250$ µm). Live/Dead staining of encapsulated 10T1/2 fibroblasts shows excellent cytocompatibility of all possible network types on day 7 of culture. Scale bar = 100 µm. c) Quantification of viability.

namic" condition) to soften the gel substrate and then cultured until the terminal timepoint of day 7. All gel conditions displayed statistically indistinguishable and high viability (>91%) (**Figure 3**), indicating that all gelation and softening conditions were mild and cytocompatible, in accordance with previous reports.[32–34,55,56]

### 2.4. IPN formation enables spatiotemporal control over mechanical properties

Sortase-mediated reversible modulation of mechanics has been reported previously;[34] however, prior reports have not demonstrated spatial control over mechanical properties, nor complete cell recovery following 3D culture. We leveraged the IPN design to spatially control thiol-ene polymerization via mask-based lithography, yielding highly defined mechanical patterns that could then be subsequently removed using 4S9 (**Figure 4a**). The lack of remaining fluorescence observed in the FAM channel indicated the complete removal of the thiol-ene network, further validating our initial release experiments (Figures 4b and 2d). To measure patterned Young's moduli pre- and post-4S9 treatment, gels were covered with a rough photomask hiding half of the gel and exposed to light; AFM indentation measurements were then taken on both halves of the gel. Subsequently, the gels were treated with 4S9, and again, Young's moduli measurements were taken on both sides. Prior to 4S9 treatment, the exposed regions exhibited Young's moduli of 3258 ± 510 Pa, whereas the nonexposed regions were 1061 ± 320 Pa, and post-treatment the previously patterned regions dropped to 838 ± 54 Pa, while the nonexposed regions remained at 1048 ± 490 Pa (Figure 4c). While our chosen gelation chemistries permit the one-pot formation of an IPN, an alternative strategy is to diffuse photo cross–linkable monomers into a pre-formed hydrogel prior to photostiffening.[57] With this in mind, we sought to reversibly cycle between a single network hydrogel and a spatially patterned IPN system. 24 h post SPAAC gel formation, we incubated the gels in thiol-ene components for 4 h at 37 °C, and then selectively exposed the gel to photomasked light to yield well-defined patterned thiol-ene polymerization (Figure 4d). The next day, the patterns were removed via 4S9 treatment, converting the IPN back to a single network with no thiol-ene network components remaining. We then repeated the patterning process, successfully converting our single network SPAAC gel back into an IPN system via thiol-ene polymerization, which proved successful. As the second IPN leaves few or no thiol-ene components behind, this process could theoretically be repeated indefinitely, unlike in a previously reported single network system where thiol-ene reactive handles were finite.[50] We note, however, that diffusing sortase and thiol-ene network components in and out of the gel is not instantaneous, necessitating diffusion times that scale with gel geometry and may place practical limits on network cyclability.

Previous reports indicated the photoinitiator lithium phenyl-2,4,6-trimethylbenzoylphosphinate (LAP) to be sensitive to two-photon-based activation;[58–60] thus, we hypothesized that our IPN system could enable the creation of complex 3D thiol-ene structures supported by the surrounding SPAAC matrix. Since LAP is only weakly two-photon active, we utilized rhodamine B as a photosensitizer in conjunction with the photoinitiator to

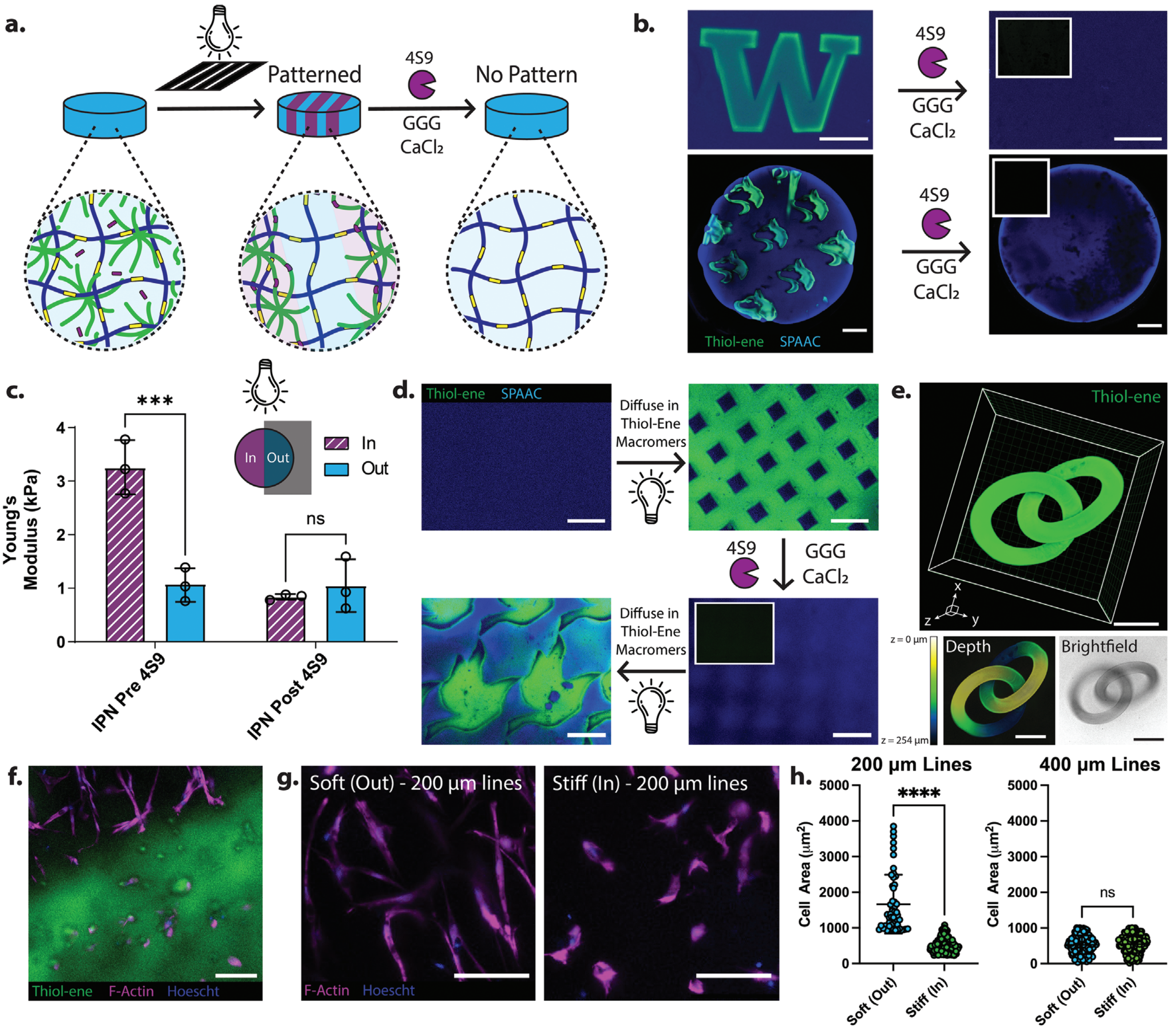

**Figure 4.** Interpenetrating networks can be reversibly and spatiotemporally patterned. a) Schematic depicting stepwise patterning and pattern removal. Soluble monomeric precursors can be mixed together in a one-pot mixture. SPAAC stepwise network formation occurs spontaneously, while thiol-ene polymerization can be spatially controlled photolithographically. Subsequently, thiol-ene patterns are removed with sortase 4S9 treatment. b) Stiff patterns in a bulk hydrogel are enabled by localized thiol-ene polymerization and can be removed by 4S9 treatment. Insets depict no fluorescence is visible in the FAM channel (thiol-ene network) post enzymatic treatment. Top scale bars = 200 µm, bottom scale bar = 1 mm. c) AFM measurements of half-patterned gels. "In" denotes a stiff region exposed to light, whereas "out" denotes the covered, non-exposed region. Two-Way ANOVA, ***$p$ = 0.0002. d) IPN design allows for reversible patterning of mechanics. Thiol-ene gel components can be diffused into single network at later time points for mechanical patterning and can be reversibly removed and reinstated by rounds of 4S9 degradation and photopolymerization. Scale bar = 250 µm. e) Intricate IPN formations can be patterned using multiphoton laser-scanning lithography and visualized both in fluorescent channels, as well as in the brightfield view. Bottom left is a depth-coded image, with yellow representing closer to the top of the z-stack, and blue representing bottom of the z-stack. Scale bars = 200 µm. f) hMSCs encapsulated in stiffness-patterned hydrogels. Image shows the interface of stiff and soft regions. Scale bar = 100 µm. g) hMSCs in soft (left) versus stiff (right) regions of patterned hydrogel. Scale bar = 100 µm. h) Quantification of cell area in soft and stiff regions in line patterns of different thicknesses. Unpaired t-test, ****$p < 0.0001$. $N$ = 3 gels per patterning condition.

photopolymerize the second network in a set of intertwining rings via laser-scanning multiphoton lithography (Figure 4e, Figure S3, Supporting Information). Interestingly, due to changes in refractive index between the two gel types, these patterns can be visualized in brightfield. Based on optical limitations, the smallest patternable feature here was 0.88 µm × 0.88 µm × 1 µm, $x \times y \times z$ respectively; image analysis showcased similar resolutions obtained for IPN formation, though we note the ≈2 µm optical sectioning limit in the $z$ dimension imposed during confocal imaging analysis. Such complexity in patterned stiffness is currently not readily obtained via other additive methods, including conventional digital light projection, extrusion-based, and volumetric 3D printing.

Next, we asked whether patterns in gel stiffness could elicit spatial changes to cellular morphology. Human mesenchymal stem cells (hMSCs) were encapsulated in IPNs featuring 200 or 400 µm-wide line patterns and cultured for 7 days, at which point they were fixed and stained with phalloidin to visualize cytoskeletal area (Figure 4f,g). Curiously, hMSC morphology varied with pattern width: for the narrower line patterns, cells in the softer SPAAC regions ("out" of pattern) were significantly larger compared to those in the stiffer IPN regions ("in" pattern). Surprisingly, cells aligned perpendicularly to the pattern, bridging the entire soft region to touch the stiffer regions (Figure S5a, Supporting Information). However, in the wider line patterns, which may more closely resemble a bulk gel on the cellular scale, we saw no significant change in cell spread area (Figure 4h, Figure S5b, Supporting Information) between the two regions. We attribute these results to differential swelling of the smaller pattern due to cell remodeling, as opposed to intrinsic properties of the gel, as we did not see statistically significant differences in pattern swelling after 7 days of incubation in full serum media as compared to PBS in acellular gels (Figure S6, Supporting Information).

### 2.5. Time-dependent softening of the matrix controls hMSC spreading and fate

We next hypothesized that softening at different timepoints throughout the culture period would temporally control cell spreading and fate. To test the first hypothesis, we encapsulated hMSCs in the stiffest IPNs (5 mM PEG-NB: 20 mM dicysteine) and single network SPAAC gels. A subset of the IPNs were softened on day 3 or day 5; all gels were fixed on day 7 (**Figure** 5a). Similar to the patterned 400 µm-wide line gels, we observed that spreading area and eccentricity in SPAAC gels as compared to the IPNs were not statistically significant (Figure 5b–d), with cells in SPAAC gels exhibiting slightly larger spread areas (385 ± 80 µm$^2$) compared to those in the IPNs (347 ± 40 µm$^2$) with only slightly more branched morphologies. We noted that hMSCs proliferated more in the soft networks as compared to the other conditions as measured by Ki67 staining (Figure S7, Supporting Information), potentially limiting their spreading time. Upon softening of the IPNs, hMSCs became highly branched and stellate, with cells exhibiting very prominent protrusions. Surprisingly, cells cultured in a stiff gel for 5 days displayed significantly higher spread areas (570 ± 47 µm$^2$) as compared to SPAAC gels and IPNs, but not compared to Day 3 (442 ± 45 µm$^2$) (Figure 5b,c), and significant increases in eccentricity as compared to IPNs (Figure 5d). The same behavior was confirmed with 10T1/2 fibroblasts (Figure S8, Supporting Information), where extended culture in a stiff matrix prior to softening elicited robust spreading. This delayed spreading response could in part be due to increased cell-generated stresses in the stiff matrices, which upon softening, may result in increased matrix displacement and protrusion formation.[61,62] However, another potentially confounding factor that drastically impacts cell morphology is gel swelling:[63] indeed, the SPAAC and dynamic gels swell more compared to the IPN gels (Figure S6a–c, Supporting Information). Studies comparing swelling and non-swelling hydrogels have previously demonstrated large differences in hMSC spreading, which can be dictated by the axis of swelling.[64] In our case, while the degree of swelling was not biologically significant, the induction of a swelling cue at a specific time point may have a significant impact on cellular morphology.

Given the previous results, we questioned whether this surprising spreading phenomenon could be due to the differential translocation of YAP/TAZ as part of the Hippo signaling pathway. To that end, we designed a tdTomato hMSC reporter line based on the Signalome reporter system for YAP/TAZ, which gives a live output of the transcriptional coactivators' translocation but does not introduce exogenous YAP/TAZ that may disrupt signaling processes.[65] In this system, the expression of tdTomato is driven by TEAD binding to the GTIIC transcriptional enhancer, downstream of interactions between TEAD and YAP/TAZ (Figure S9, Supporting Information).[66,67] We repeated the dynamic softening experiment with this modified cell line and live-imaged each gel on days 1, 3, 5, and 7; gels softened on days 3 and 5 were first imaged on their respective days of softening, and then treated with 4S9. Initially, cells displayed a low level of tdTomato fluorescence, which began to increase with time spent in the IPN conditions, with a sharp increase between days 3 and 5 of culture (Figure 5e,f). By day 7 of culture, dynamic gels softened on day 3 saw a small drop in tdTomato intensity but did not return to the levels of cells cultured in soft SPAAC gels; in a more pronounced fashion, the gels softened on day 5 exhibited the highest fluorescent reporter activity on day 7, yet not statistically significant from IPN gels, with accordingly high cell spreading (Figure 5f, Figure S9, Supporting Information). The elevated Hippo signaling in static stiff and dynamic gels in comparison to static soft gels may signify a conserved memory of the previous stiff environment and may help facilitate the formation of longer protrusions. While YAP/TAZ translocation has been shown to be fast (on the order of min),[67,68] downstream signaling and cytoskeletal reorganization in 3D may occur on much longer scales. Previous studies demonstrated that unlike in 2D, YAP/TAZ nuclear translocation is inversely proportional to 3D matrix stiffness; however, cell spreading and actomyosin contractility in degradable matrices are proportional to YAP/TAZ translocation.[69] Given that our IPN and SPAAC materials are not as stiff as the materials studied by Caliari et al. (upward of $E \approx$ 20 kPa), our experimental results are more comparable to their results in the soft to medium stiffness groups ($E \approx$ 1–5 kPa), which similarly displayed small to large protrusions in 3D. Additionally, as the SPAAC gels facilitated higher rates of proliferation and potentially more material remodeling, YAP/TAZ signaling could be driven by decreased mechanical traction in this system.[70] Studies with extended culture times could prove useful to further examine this phenomenon.

Finally, to better benchmark our system with other similar platforms,[14,64,71] we questioned whether the material stiffness could bias hMSCs differentiation. hMSCs were encapsulated and cultured in bipotential (50:50 adipogenic/osteogenic) media for 7 or 14 days. On day 7, Oil Red O staining demonstrated some adipogenesis across all conditions, with the SPAAC condition being the highest (Figure 5h, Figure S10, Supporting Information), but no osteogenesis was observed. By day 14, all groups had robust lipid droplet formation, but only the IPN group displayed some,

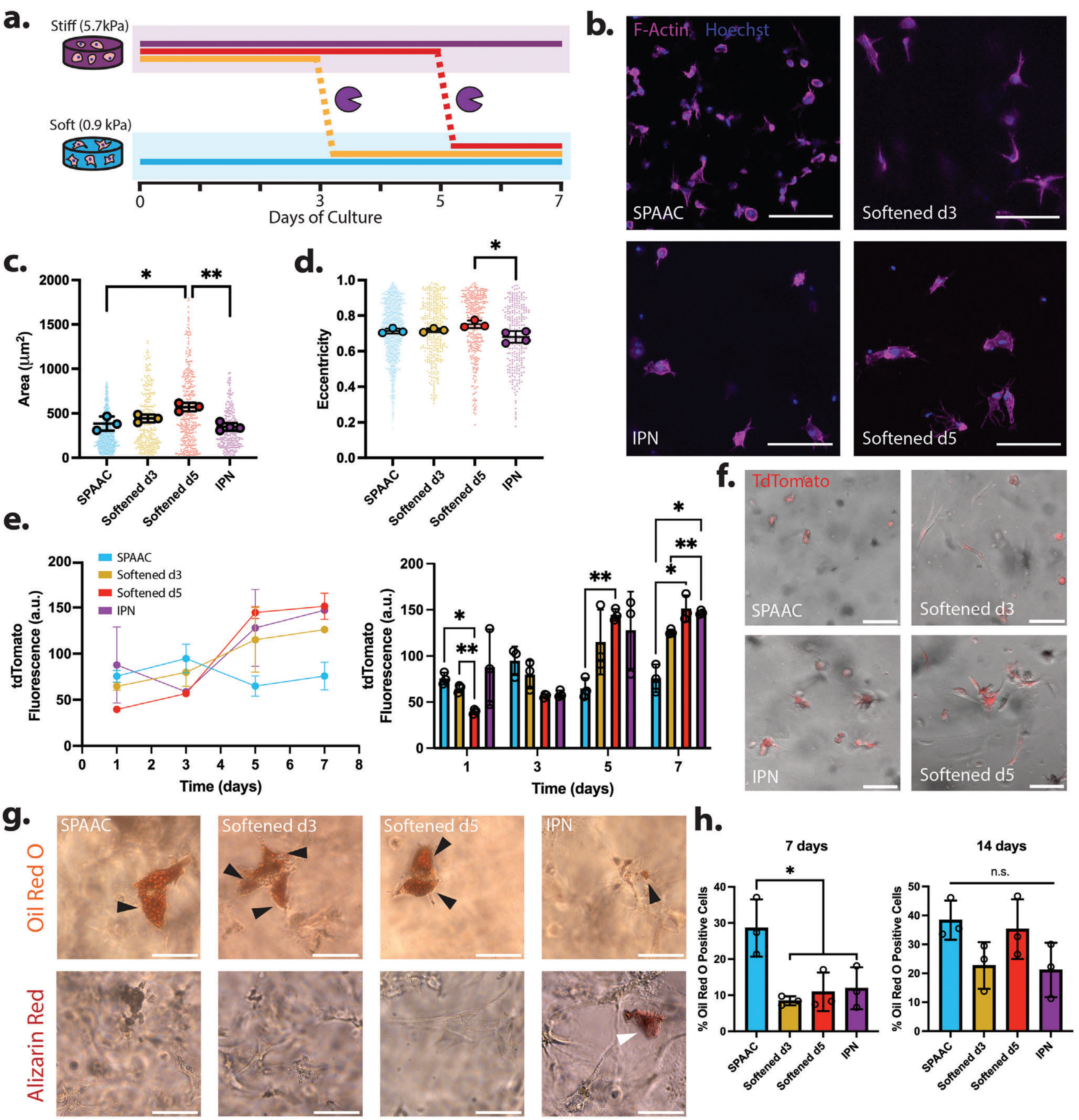

**Figure 5.** Time-dependent softening controls hMSC spreading behavior. a) Experimental setup. hMSCs were encapsulated in static or dynamic IPNs or SPAAC networks. Dynamic IPNs underwent softening on day 3 ("softened d3") or day 5 ("softened d5"). b) Actin and nuclear staining reveal distinct morphologies amidst experimental groups. Scale bar = 100 µm. c) Quantification of cell area. Small dots indicate individual cell values, whereas larger circles indicate per gel average. Statistics were conducted on the per-gel averages. One-Way ANOVA, Tukey's post-hoc test, $^*p = 0.0105$, $^{**}p = 0.0021$. d) Quantification of eccentricity. One-Way ANOVA, Tukey's post-hoc test, $^*p = 0.0123$. e) Live imaging of tdTomato intensity as a function of time in line (left) and bar (right) plot form. Dynamic IPN gels were imaged prior to degradation on their respective degradation days. Two-Way ANOVA, Tukey's post-hoc test. $^*p < 0.05$, $^{**}p < 0.01$. f) Representative images of hMSCs expressing tdTomato upon TEAD binding events occurring on day 7 of encapsulation. Scale bar = 100 µm. g) Representative photos of hMSCs on day 14 stained for Oil Red O (adipogenesis; top) and Alizarin Red (osteogenesis; bottom). Black arrows denote fat droplets, and white arrows denote calcium deposits. Scale bar = 50 µm. h) Quantification of Oil Red O positive cells on days 7 and 14 of culture. One-Way ANOVA, Tukey's post-hoc test, $^*p < 0.05$.

albeit minimal, calcium depositions (Figure 5g,h). As our materials are quite soft in comparison to those used for osteogenic differentiation,[72,73] it is unsurprising that none of the terminally softened conditions supported any osteogenic differentiation.

### 2.6. Transcriptomic and metabolic analysis of Caco-2 cells subjected to time-dependent softening

An added and important advantage of our dynamically softening bulk hydrogels is that encapsulated cells can be recovered from the gels in a near "biologically invisible" manner and subsequently processed in downstream cellular assays. Toward this end, we investigated cellular mechanomemory in our system with RNAseq. One area where the concept of mechanomemory has recently gained traction is in cancer therapies;[18] in particular, there has been growing interest in examining how modulating mechanics of the tumor microenvironment via antifibrotic treatments could improve outcomes in colorectal and pancreatic ductal adenocarcinoma.[17,74,75] Of note, Shen et al. reported that altering the mechanical properties of metastatic colorectal tumor stroma by inhibiting fibroblast matrix deposition, improved patient response to targeted therapies;[17] yet, a full mechanistic explanation remains elusive. Moreover, studies in hMSCs and gastric cancer cell lines have shown that cells retain the memory of their previous mechanical environments, and that dosage time greatly affects the regulation of YAP/TAZ and downstream signaling pathways;[6,25,71] however, the mechanomemory of colorectal cancer has yet to be assayed.

The Caco-2 colorectal adenocarcinoma cell line was selected as a model cell line for its popularity as a model for human intestinal mucosa[76] and as a well-differentiated tumor model.[77] We encapsulated Caco-2 cells in the baseline IPN formulation (3 mм PEG-NB: 12 mм dicysteine: 3 mм PEG-BCN: 12 mм diazide) which matches the stiffness of primary, premetastatic colon cancer tissue collected from patients, as well as in soft, single network SPAAC gels, the moduli of which correspond to that of healthy colon tissue.[52,78] A subset of the IPN gels were softened, as in previous experiments, on day 3 and day 5. On day 7, all gels were fully degraded with a cocktail containing both 2A9 and 4S9 to mitigate the potential effects of sortase treatment on genomic perturbation (**Figure 6**a). Collected cells were lysed for global transcriptome quantification by RNAseq, which identified and quantified over 15 000 genes from the human genome.

By principal component analysis (PCA) (Figure 6b), the first principal component (PC) accounted for a relatively large fraction (54%) of sample variance and could distinguish readily between soft and stiff conditions. PC2 (28%) resolved the differences between static (soft and stiff) and dynamic (day 3 and day 5 conditions), however the day 3 and day 5 conditions clustered together, suggesting the day of softening is not as impactful as the bulk modulation of mechanics. To delve further into the various comparisons, we first chose to compare the two static, baseline controls—soft (SPAAC) versus stiff (IPN); we observed 1116 genes significantly upregulated and 131 downregulated (fold change > |2|) (Figure 6c). Over-representation analysis (ORA) via MSigDB identified terms related to cell division and metabolism, as well as MYC and mTOR signaling (Figure S11, Supporting Information). Certain previously established mechanosensitive genes such as *RHOC* and *LIMK1* were upregulated in the soft condition, suggesting higher cytoskeleton reorganization activity, which was also supported by upregulation of matrix and metalloproteinase genes, such as *COL18A1*, *COL4A2*, *MMP15*, *MMP24*, and *ADAM15* (Figure 6c).[79–81] We also observed significant up and downregulation of genes up and downstream of the AKT1 and MAPK pathways, which are key regulators of proliferation, invasion, metabolism, cytokine production, and survival (e.g., *AKT1*, *MAPK3*, *EGR1*, *EREG*, *ERBB4*, *CXCR4*).[82–85] Some of these genes have been shown to interact with the Hippo pathway; for instance, AKT1 phosphorylates YAP1, promoting its cytosolic retention, while EREG and ERBB4 are upstream of the MAPK/AKT pathways, and may also promote YAP1 nuclear localization.[84,85] While many common mechanosensitive genes in the Hippo pathway did not exhibit high fold changes in expression, *YAP1*, *ROCK1*, and *ROCK2* expression were significantly lower in the soft conditions (FDR $< 0.05$, fold change $-1.44$, $-1.51$, $-1.53$, respectively), as has been previously shown in other biomaterial platforms, both 2D and 3D.[6,71]

When we compared dynamic (day 3 and day 5) versus static (IPN and SPAAC) conditions, we saw striking differences in gene expression (Figure 6d). ORA of the differentially expressed genes returned pathways such as "cholesterol homeostasis", "mTOR signaling", "hypoxia" and "EMT" as highly significant (Figure 6e). Similarly, we conducted gene-set enrichment analysis (GSEA),[86] which takes into account all differences in gene expression even below the threshold required for ORA, on the same comparison, and saw downregulation of cholesterol homeostasis and EMT-related genes in dynamic conditions, with similar trends in glycolysis genes (Figure S12, Supporting Information). We then conducted ORA on differentially expressed genes in all comparisons (Figure S11, Supporting Information). While the comparison for day 3 versus day 5 did not yield any significant pathways, all other comparisons showed enrichment of many similar pathways: mTOR and MYC-related signaling pathways were highly enriched in 5 out of 5 and 4 out of 5 comparisons, respectively. We observed striking differences in these signaling pathways, especially between the dynamic conditions compared to stiff or soft (Figure S13, Supporting Information). As both of these pathways are downstream of PI3K-AKT and MAPK activity, it is unsurprising that they are highly affected by mechanical stimuli, and have previously been demonstrated as such.[87–90] The protooncogenic protein MYC has been demonstrated to regulate global metabolic reprogramming and plays a pivotal role in 5-fluorouracil resistance in colorectal cancer.[91,92] Many MYC-associated genes were most highly expressed in the stiff condition, while the dynamic conditions displayed the lowest expression of these genes (Figure S13, Supporting Information), similar to a recent report by Nguyen and Lin in COLO-357 spheroids,[93] potentially signifying that modulating the mechanical environment plays a major role in suppressing this signaling axis.

Given these shifts in signaling pathways that regulate metabolic activity on the transcriptome level, we hypothesized that these changes would be reflected in real-time bioenergetic measurements. To test this, we measured the cellular redox capacity of encapsulated cells on day 7 in different conditions using the RealTime-Glo assay (Promega). Here, we observed a significant increase in metabolic activity in the Caco-2 cells encapsulated in the static soft SPAAC gel as compared to the dynamic

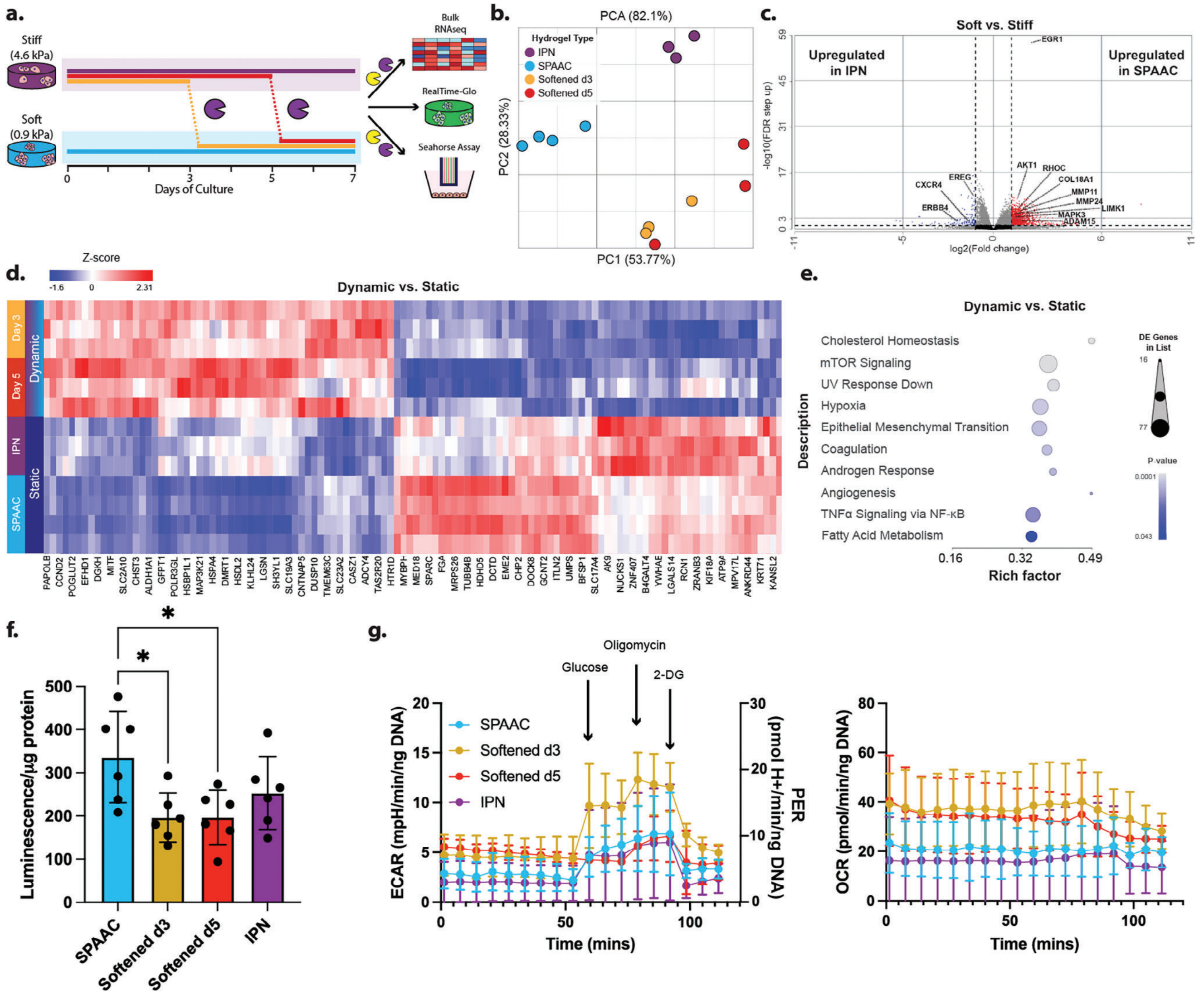

**Figure 6.** Transcriptomic and metabolic analysis of Caco-2 cells in static and dynamically softened hydrogels. a) Experimental setup. b) PCA plot from bulk RNAseq data. c) Volcano plot of gene expression profile in SPAAC versus IPN hydrogels. Red = upregulated genes in SPAAC condition, blue = downregulated genes in SPAAC condition. d) Top upregulated and downregulated genes for dynamic versus static comparison. e) Enriched MSigDB gene sets among differentially expressed genes for dynamic versus static comparison. f) Day 7 RealTime-Glo$^{TM}$ in gel luminescence measurements as a proxy for cellular redox capacity. Raw luminescence values were normalized to total lysed protein content. One-Way ANOVA, Tukey's post-hoc test, *$p < 0.05$. g) Bioenergetic profiles of released Caco-2 cells (ECAR: extracellular acidification rate, PER: proton efflux rate, OCR: oxygen consumption rate). $N \geq 3$ for all conditions.

conditions (Figure 6f). High levels of NADPH to power biosynthetic reactions and scavenge radical oxygen species have been linked to the rapid growth of various cancers, including colorectal cancer; presumably, this cofactor is also responsible for donating electrons to the prosubstrate, thus reducing it and leading to higher rates of luminescence.[94,95] Bolstering this finding, the colonies in the SPAAC gels were significantly larger than those in the IPN condition, displaying more cells per colony compared to all conditions (Figure S14, Supporting Information).

A previous study demonstrated that Caco-2 cells modulate relative rates of oxidative phosphorylation and glycolysis depending on their dimensionality, and demonstrated that soft 3D cultures tend to be less glycolytic than 2D.[96] These studies, however, did not assay how 3D culture stiffness may affect these relative rates. To fill this knowledge gap, we next asked whether hydrogel mechanics influenced the cells' glycolysis rates and whether they could retain the memory of their former 3D environment. On day 7 of the assay, cells were released from their respective hydrogels and briefly allowed to adhere to the bottom of a multiwell plate to form a 2D monolayer. Using a Seahorse XF Pro Analyzer, we assayed each culture's real-time extracellular acidification (ECAR) and oxygen consumption rate (OCR) (Figure 6g). Intriguingly, we saw that the cells in gels softened on day 3 displayed the highest rates of glycolysis, with more pronounced spikes in ECAR when exposed to glucose and oligomycin, an inhibitor of ATP synthase, which effectively pushes the cells toward fully glycolytic respiration. Cells formerly in gels softened on day 5 displayed similar rates to those from static gels, potentially signifying that the transition into a higher glycolytic state may require more time spent in a softer gel, following the gradient-like trends shown in the RNAseq analysis. On the other hand, OCR data showed a distinction between dynamic and static gels, which is slightly in contradiction with the RealTime-Glo assay results; however, this switch could be induced by changes in cellular morphology as they transitioned from a 3D colony to a single-cell suspension. We note that assays such as these are particularly challenging to conduct on 3D hydrogels due to the small chamber size and hydrogel networks affecting the rates of diffusion of small molecules; thus, our method allows for the release of intact, live cell populations for 2D analyses.

We finally examined how these changes in mechanical properties affect known mechanosensitive and ECM-related genes previously shown in 3D biomaterial platforms (Figure S13, Supporting Information).[25] We noted differences in gene expression among static and dynamic conditions, as well as differences between the static soft and stiff conditions. Further, we noticed a gradient-like response (middle and right side of heatmap) for a subset of MMP (specifically many membrane-bound subtypes) and collagen and laminin genes, with soft gels having the highest expression, followed by intermediate expression in the day 3 condition, and lower expression in the day 5 condition, similarly to the stiff condition. ECM remodeling and deposition are complex and multistep processes, known to take place on longer timescales than acute intracellular signaling cascades, potentially explaining the range in response across multiple days.[97–99] In sum, 4D-tunable biomaterials, such as our IPN system, are key to exploring these intricate, interwoven, and dynamic biological phenomena. Our IPN design is the first fully synthetic interpenetrating network system that enables reversible and spatially controlled mechanical modulation with subsequent bioorthogonal cell recovery. The combination of orthogonal single network formation and degradation reactions opens powerful doors for investigating the role of matrix mechanics on many biological systems.

## 3. Conclusion

3D models that can modulate native tissue mechanics in a spatiotemporally defined manner could prove useful in studying the effects of ECM stiffness on drug efficacy, disease progression, and mechanomemory.[18,23] Herein, we have presented a bioorthogonal platform that allows for spatiotemporal control over Young's moduli, as well as temporal control over bulk stiffening/softening and subsequent cellular release. We engineered the stepwise formation of an IPN composed of two discrete bioconjugate chemistries which can then be reversibly stiffened through distinct bioorthogonal reactions and subsequently softened via orthogonal sortase treatments. In our design, all macromer components can be either initially present or sequentially diffused in: the SPAAC network forms spontaneously, generating a soft initial network, that can then be stiffened with spatial precision by thiol-ene photopolymerization. The IPN can be subsequently reverted back to the starting single network via sortase-mediated transpeptidation; the photopolymerization and enzymatic degradation can be repeated as one sees fit, but then the whole network can be fully degraded to recover embedded live cells in a "biologically invisible" manner - a feature not common in many current biomaterial models - for downstream analysis in assays not readily compatible with 3D culture methods.

In developing this system, we demonstrate its utility toward studying changes in cell morphology and mechanosignaling, both through live imaging, bulk transcriptomics, and metabolic analyses. Moreover, our material chemistry-based approach is generalizable: other bioorthogonal chemistries and/or enzymatic pairs may be utilized to create alternate versions of reversibly formed IPNs depending on access and need. While the networks demonstrated herein are purely elastic, there is a growing appreciation for the importance of the viscous material characteristics on cell fate; as such, our design framework could be broadened to include networks with more stress-relaxing properties, potentially by including the sortase-sensitive sequences in recombinantly expressed hydrogels or modifying natural biopolymers (e.g., alginate) with photoreactive handles.[100–106] We readily envision the extension of our method to other biological systems where mechanobiological questions are of pressing interest.

## 4. Experimental Section

*Materials*: Materials, reagents, and cell culture consumables were purchased from Sigma-Aldrich (St. Louis, MO), ThermoFisher (Waltham, MA), and ChemImpex (Wood Dale, IL) unless otherwise noted. Fmoc-protected amino acids were purchased from ChemPep Inc. (Wellington, FL). Dicysteine peptide Ac-GCRDLPESGGPQGIWGQDRCG-$NH_2$ was purchased from Genscript (Piscataway, NJ), resuspended in 10% glacial acetic acid, and lyophilized to yield aliquots of the desired mass. Poly(ethylene glycol) tetra-bicyclononyne (PEG-BCN), 8-arm PEG-norbornene, and the diazide peptide cross–linker [$N_3$-RGPQGIWGQLAETGGRK($N_3$)-$NH_2$] were synthesized and processed as previously described (Experimental Sections S1 and S2, Figure S1, Supporting Information).[33,37,40,41] pET29b expression plasmids for 2A9 and 4S9 were a generous gift from Dr. David Liu at Harvard University (Addgene plasmids #75145 and #75146). Sortase enzymes were expressed and purified as previously described (Experimental Sections S1 and S2, Figure S2, Supporting Information).[33] Caco-2 colorectal adenocarcinoma cells were a generous gift from Dr. William Grady at the Fred Hutchinson Cancer Center.

*Interpenetrating Network Hydrogel Formation*: IPNs were formed in a stepwise manner. Unless otherwise specified, all monomers and gel precursors were combined at 3 mm PEG-BCN: 6 mm diazide: 3 mm PEG-NB: 12 mm dicysteine: 1 mm lithium phenyl-2,4,6-trimethylbenzoylphosphinate (LAP; Allevi3D; Philadelphia, PA). Upon mixing, 10 µL droplets were pipetted between Rain-X-coated glass slides spaced at 500 µm. SPAAC networks were allowed to form for 20 min at 37 °C, at which point they were exposed to collimated near-UV light ($\lambda$ = 365 nm; 10 mW $cm^{-2}$; OmniCure 1500; Excelitas Technologies; Waltham, MA) for 2 min (unless otherwise specified) to drive thiol-ene polymerization. For encapsulation, gel formulations included 1 mm $N_3$-GRGDS-$NH_2$ to promote cell adhesion.

*Photorheology*: Gel formation kinetics and storage moduli (G') were analyzed on a Physica MCR-301 rheometer (Anton Paar; Graz, AT) at 25 °C with 8 mm parallel plate geometry (0.5 mm gap, 1 Hz, 1% strain). The SPAAC network was allowed to form for 1 h, at which point 365 nm light at 10 mW $cm^{-2}$ was irradiated from the bottom plate coupled to a fiber optic light guide from a multiwavelength LED light source (Mightex Systems; Toronto, ON). The frequency and strain were determined to fall within the viscoelastic range via frequency and amplitude sweeps.

*Atomic Force Microscopy Measurements*: Hydrogel solution (40 µL) was pipetted onto a Rain-X-coated glass slide with 500 µm-thick rubber spacers, on top of which were placed 18 mm-diameter thiolated glass coverslips. After gel formation, coverslips with attached gels were allowed to swell overnight in PBS. The following day, atomic force microscopy (AFM) measurements were performed on an Asylum Cypher S AFM (Oxford Instruments; Concord, MA) with a Bruker NP-O10 silver nitride cantilever (Bruker; Camarillo, CA) ($k$ = 0.35 N/m; f = 65 kHz) functionalized with 50 μm-diameter soda lime glass spherical beads (Cospheric; Santa Barbara, CA).[42] The sensitivity and the spring constant of the probe were calibrated before usage ($k = 0.22$ N m$^{-1}$) in PBS using a fused silica sample in a Peak Force QNM Sample kit (Bruker; Camarillo, CA). All measurements were taken in contact mode and approach and retraction speeds were 1.98 μm s$^{-1}$ with a trigger point of 1 V and a retraction distance of 1 μm. For each sample, 5 force maps were generated by indenting in 30 μm × 30 μm grids with 100 indentation points, collecting at least 300 fittable force curves. Three substrates were measured for each condition. To evaluate Young's moduli, indentations were fitted to a Hertzian model using the Cypher 16.14.216 software. For softened hydrogels, due to the heterogenous surface heights, samples were indented in 5 discrete locations at least 10 times, giving at least 50 measurements for subsequent analysis per substrate. For patterned hydrogels, the same procedure was used as for softened hydrogels, except that 5 discrete locations were chosen in the light-exposed regions ("in" pattern) and the non-exposed region ("out" of pattern). Three samples were measured for each condition.

*Interpenetrating Network Softening*: IPNs were softened by treating with 50 μM 4S9, 18 mM GGG, and 10 mM CaCl$_2$ for 1 h, and washed 3 × 10 mins afterward to remove degraded thiol-ene network components. For cell culture applications, GGG was resuspended in full-serum media and the pH was adjusted to ≈7; additionally, all components were sterile filtered through 0.2 μm syringe filters. Post-softening, gels were washed for 3 × 10 mins with full-serum media.

*Assaying Orthogonal Degradation of IPNs*: Hydrogels were made at the following concentrations: 3 mM PEG-BCN: 6 mM diazide: 3 mM PEG-NB: 12 mM dicysteine: 1 mM LAP. Each network was tagged with a different fluorophore: dicysteines resuspended at a 40 mM concentration were prereacted with 100 μM of AlexaFluor 488 maleimide (1:400 dye:peptide) (Click Chemistry Tools; Scottsdale, AZ) for 15 min, whereas PEG-BCN was preincubated for 15 min with 50 μM of AlexaFluor 568 azide (1:200 dye:PEG) (Click Chemistry Tools; Scottsdale, AZ). IPN hydrogels were then formed with these fluorescently tagged components and allowed to swell and wash away unreacted dye overnight. The following day, gels were treated with 50 μM of either 2A9 or 4S9, 18 mM GGG, and 10 mM CaCl$_2$ (400 μL total volume). To quantify degradation extent, 2 μL of supernatant was taken from the well at each timepoint and diluted in 98 μL of PBS in a black 96-well plate. Fluorescent values were read on a plate reader (Molecular Devices; San Jose, CA) and normalized to the final release at 12 h. To normalize the non-degrading network, the gels were treated with the other sortase variant for 1 h at the end of the experiment to fully degrade the remaining network, leaving a completely soluble mixture (e.g., an IPN analyzed for 2A9 degradation was treated at the end with 4S9 to degrade the remaining single network), the fluorescence of which was evaluated in both channels.

*Interpenetrating Network Patterning and Visualization*: IPNs were formed as described previously at 3 mM PEG-BCN: 6 mM diazide: 3 mM PEG-NB: 12 mM dicysteine: 1 mM LAP. 100 μM FAM-maleimide was additionally included to visualize the thiol-ene network. 10 μL gels were formed on Rain-X-coated glass slides with 1 mm-thick rubber gaskets. Gels were incubated at 37 °C for 20 min to form initial SPAAC networks. After initial polymerization, one glass slide was removed and replaced with a photomask to reduce diffraction during patterning. Gels were then exposed to collimated UV light ($\lambda = 365$ nm; 10 mW cm$^{-2}$; Omnicure 1500) through a chrome photomask (Photo Sciences; Valencia, CA) for 2 min, allowing for thiol-ene polymerization and formation of IPN patterns. Following patterning, gels were soaked in 10 μM Cy5-N$_3$ (Click Chemistry Tools; Scottsdale, AZ) for 2 h at 37 °C to label the SPAAC network and then washed 3 × 1 h in PBS. For cellular applications, the SPAAC network was not fluorescently labeled, and gel formulations included 1 mM N$_3$-GRGDS-NH$_2$ to promote cell adhesion. Imaging was performed using the Leica Stellaris confocal microscope.

*Two-photon Patterning and Visualization*: IPNs were formed as described previously (3 mM PEG-BCN: 6 mM diazide: 3 mM PEG-NB: 12 mM dicysteine: 1 mM LAP), but with 25 μM Rhodamine B included as a photosensitizer. Gels were formed between Rain-X-coated glass coverslips and slides with 1 mm-thick rubber gaskets that enclosed the gel in an air chamber. Gels were patterned using a Thorlabs Bergamo II 2-photon confocal microscope equipped with a Coherent Chameleon Discovery NX tunable femtosecond laser and an Olympus liquid-immersion objective (25×, numerical aperture = 0.95), controlled via ScanImage software (MBF Bioscience; Williston, VT).[43] The imported image sequence (field of view = 450 μm × 450 μm × 234 μm) was patterned at $\lambda = 780$ nm in the z-direction (resolution = 0.88 μm/px × 0.88 μm/px × 1 μm/px, pixel dwell time = 3.2 μs, 210 mW, 50 scan repeats) (Figure S3a, Supporting Information).[43] Following patterning, gels were soaked in 10 μM Cy5-N$_3$ (Click Chemistry Tools; Scottsdale, AZ) for 2 h at 37 °C to block any unreacted BCN groups, washed 3 × 1 h in PBS, and then incubated with 50 μM AZDye 488-tetrazine (Click Chemistry Tools; Scottsdale, AZ) for 2 h at 37 °C to visualize the thiol-ene network. Gels were washed overnight in PBS and then imaged on a Leica Stellaris confocal microscope. A 3D model was reconstructed in IMARIS (Oxford Instruments; Abingdon, Oxfordshire, UK) and the depth-coding functionality on ImageJ was utilized to process individual z-stacks for visualization (Figure S3b, Supporting Information).

*Cell Culture*: 10T1/2 fibroblasts were cultured in Dulbecco's Modified Eagle Medium (DMEM) supplemented with 10% fetal bovine serum (FBS) and 1X Penicillin-Streptomycin (PS) in a standard 37 °C, 5% CO$_2$ cell culture incubator. Cells were passaged 1:10 upon reaching 80% confluency. Experiments were conducted with 10T1/2 cells below passage 15. Human mesenchymal stem cells (hMSC) were purchased from RoosterBio, Inc. (Frederick, MD) and grown in low-glucose DMEM supplemented with 10% FBS and 1X PS and passaged similarly to 10T1/2 cells; all experiments were conducted with cells below passage 5. For differentiation studies, encapsulated cells were cultured in bipotential 50:50 adipogenic:osteogenic media. Adipogenic media consisted of low-glucose DMEM with 10% FBS, 1X PS, 5 μg mL$^{-1}$ insulin, 1 μM dexamethasone, 0.5 mM 3-isobutyl-1-methylxanthine, and 200 μg mL$^{-1}$ ascorbic acid. Osteogenic media consisted of low-glucose DMEM with 10% FBS, 1X PS, 100 nM dexamethasone, 50 μg mL$^{-1}$ ascorbic acid, and 10 mM $\beta$-glycerophosphate. Caco-2 cells were cultured in Eagle's Minimum Essential Medium (EMEM) supplemented with 20% FBS and 1X PS and passaged similarly to the other cells; all experiments were conducted with cells below passage 15.

*Live/Dead Imaging*: 10T1/2 fibroblasts were encapsulated in gels at a concentration of 2 × 10$^6$ cells mL$^{-1}$ and cultured for 7 days. Dynamic IPNs were treated on day 3 with 4S9. Cell viability was assayed by live–dead staining with calcein AM and ethidium homodimer (EtHD). Hydrogels were incubated in live–dead staining solution (2 μM calcein and 4 μM EtHD in PBS) for 1 h prior to confocal imaging. Live–dead count was quantified from 250 μm max intensity projections (MIP) using IMARIS.

*hMSC Staining and Analysis*: hMSCs were encapsulated in gels at a concentration of 2 × 10$^6$ cells mL$^{-1}$ and cultured for 7 days in either bulk or patterned gels. On day 7, gels were fixed by treatment with 4% paraformaldehyde (PFA) for 1 h at room temperature, washed 3 × 10 min with tris-buffered saline (TBS), and permeabilized for 30 min with 0.5% Triton X-100 in TBS. Subsequently, actin was labeled with 1:400 Phallodin-532, and nuclei– with 1:1000 Hoechst 33342 in TBS. Gels were rinsed in TBS and imaged on a Leica Stellaris confocal microscope. Cell area and eccentricity were analyzed from 100 μm MIPs with Cell Profiler 4.0.[44] For differentiation assays, hMSCs were encapsulated in gels at a concentration of 2 × 10$^6$ cells mL$^{-1}$ and cultured for 7 or 14 days in bipotential media. On day 7 or day 14, gels were fixed with 4% PFA for 1 h at room temperature and washed for 3 × 10 min with PBS. For adipogenic staining, gels were incubated in 0.3% Oil Red O solution at room temperature (3 × 45 min) with an intermittent PBS wash (10 min), and then finally washed with PBS overnight. For osteogenic staining, gels were incubated in Alizarin Red solution (40 mM in DI H$_2$O) for 4 h at room temperature. Gels were then washed with DI H$_2$O overnight. Gels were imaged on an Echo Revolution microscope. Percent Oil Red O positive cells were quantified by dividing the number of red stained cells by the total cell number based on DAPI counterstaining.

Lentiviral Construct Assembly and Transduction: YAP/TAZ-TRE-mStrawberry reporter was a gift from Ravid Straussman (Addgene plasmid # 158682). From this plasmid, polymerase chain reaction (PCR) was used to amplify the backbone and the TEAD-binding sequence repeats, TRE/GTIIC. The resultant PCR product was reassembled into a tdTomato-containing vector via Gibson assembly (NEB) with a tdTomato insert (sequence ordered as a codon-optimized gBlock from IDT) and transformed into NEB Stable *E. Coli*.

Human embryonic kidney (HEK293T) cells were plated at ≈40% confluency and allowed to adhere to tissue culture plastic overnight. Fresh media was added, and then HEKs were transfected with envelope plasmid pMD2.G (Addgene #12259), packaging plasmids pMDLG/pRRE (Addgene #12251) and pRSV-REV (Addgene #12253), and the YAP/TAZ-TRE-tdTomato plasmid using Lipofectamine 2000. Cells were cultured for 2 days post-transfection, and virus-laden media was harvested. Viral media was filtered (0.45 µm) and tested using a lentiviral titration card (ABM Biologics; Richmond, BC, CA). Active lentivirus was concentrated by mixing viral media with 4X lentiviral concentration solution (40% w/v PEG-8000, 1.2 M NaCl), vigorously shaking for 60 s, and agitated overnight at 4 °C. The following day, flocculated lentiviral particles were pelleted at 1600 × g for 60 min at 4 °C, and the supernatant was aspirated. Pellet was resuspended at 10× relative to the initial viral media volume in PBS.

hMSCs were plated at ≈40–60% confluence the day before the transduction and allowed to adhere overnight. The following day, their media was replenished and supplemented with 8 µg mL$^{-1}$ polybrene and the prepared lentivirus. Transduction was allowed to occur overnight, then viral media was aspirated and replaced with regular culture media. After 2 days in recovery, hMSCs were exposed to 4 µg mL$^{-1}$ of blasticidin and were selected for 7 days. Selection media was replaced every 3–4 days. After selection, hMSCs were expanded and used for encapsulation.

For live-cell imaging of TEAD-binding activity, transduced hMSCs were encapsulated at a concentration of 2 × 10$^{6}$ cells mL$^{-1}$ and cultured for 7 days. Throughout the experiment, cells were live imaged on days 1, 3, 5, and 7 with 50 µm thick z stacks in 3 discrete locations per gel for quantification of tdTomato intensity with CellProfiler 4.0. Dynamic gels were treated with 4S9 immediately post-imaging on their respective days (e.g., dynamic day 3 gels were first imaged on day 3, then softened). Following imaging on day 7, gels were fixed and labeled with phalloidin-532 and Hoechst 33342.

*Bulk RNA Sequencing*: Caco-2 cells were encapsulated in gels at a concentration of 10 × 10$^{6}$ cells mL$^{-1}$ and cultured for 7 days, with a subset of IPNs being softened on days 3 and 5. To induce full gel dissolution at the end of the tissue culture period, all gels were treated with 50 µm 4S9, 50 µm 2A9, 36 mm GGG, and 1 mm CaCl$_2$ for 30 min. Cells were pelleted, washed 1X in ice-cold PBS, and lysed in TRIZol reagent. RNA was isolated from lysed samples using the Direct-Zol RNA microprep kit (Zymo Research; Irvine, CA), snap-frozen in liquid nitrogen, and stored at 80 °C until further use. Prior to sequencing, RNA integrity (RIN) was evaluated using the 4200 TapeStation System (Agilent; Santa Clara, CA); all RIN values were greater than 8. mRNA was converted into dual-indexed cDNA libraries using the Illumina Stranded mRNA Prep and Ligation kit (Illumina; San Diego, CA) and sequenced on the Illumina NextSeq 2000 Platform (30 million clean paired-end reads per sample). Data analysis was conducted on the Partek Flow Software (Partek; St. Louis, MO). Reads were aligned using the STAR package,[45] annotated to the human genome (Ensembl Transcripts release 109), and evaluated for differential expression via DESeq2.[46] A false discovery rate (FDR) of 0.05 was used as a cut-off for significant differences in expression. Gene set enrichment analysis was performed using the Molecular Signatures Database (MSigDB).[47]

*RealTime-Glo Assay*: Caco-2 cells were encapsulated in gels at a concentration of 2 × 10$^{6}$ cells mL$^{-1}$ and cultured for 7 days, with a subset of IPNs being softened on days 3 and 5. On day 7, all gels were incubated for 1 h with RealTime-Glo components (Promega; Madison, WI) at 37 °C, and luminescence was measured on a plate reader (Molecular Devices; San Jose, CA). Following this, cells were released from each individual gel by treatment with 50 µm 4S9, 50 µm 2A9, 36 mm GGG, and 1 mm CaCl$_2$ for 30 min. Cells were pelleted for 5 mins at 200 g, washed once with ice-cold PBS, pelleted again, and then lysed in mammalian protein extraction reagent with complete protease inhibitor. The total protein amount was determined via bicinchoninic acid (BCA) assay. Luminescent values were normalized by total protein content.

*Seahorse XF Glyco Stress Test*: The Seahorse XF Glyco Stress Test was performed according to the manufacturer's instructions on a Seahorse XF Pro Analyzer (Agilent; Santa Clara, CA). Caco-2 cells were encapsulated in 20 µL gels at a concentration of 10 × 10$^{6}$ cells mL$^{-1}$ and cultured for 7 days, with a subset of IPNs being softened on days 3 and 5. On day 7, cells were released from the gels with 50 µm 4S9, 50 µm 2A9, 36 mm GGG, and 1 mm CaCl$_2$, immediately pelleted, and resuspended in EMEM with 20% FBS and plated on a Seahorse XFe96/XF Pro Cell Culture microplate (Agilent; Santa Clara, CA), where each well corresponded to one gel population. The cells were allowed to adhere for 4.5 h prior to the beginning of the assay. 1 h prior to measurements, cells were gently washed with XF Base Medium with 2 mm L-Glutamine, but without glucose and pyruvate, and incubated in a CO$_2$-free incubator at 37 °C for 1 h to establish equilibrium. The assay was conducted as per the supplier's documentation. To normalize the extracellular acidification rate (ECAR) and oxygen consumption rate (OCR) at the end of the experiment, cells were lysed to determine total DNA content with a Quant-iT PicoGreen dsDNA assay.

*Statistical Analysis*: Unless otherwise noted, data and statistical analysis were conducted on GraphPad Prism 7.0.

## Supporting Information

Supporting Information is available from the Wiley Online Library or from the author.

## Acknowledgements

This work was supported by a Faculty Early Career Development (CAREER) Award (DMR 1652141 to C.A.D.), a standard award (DMR 1807398, C.A.D.), and Graduate Research Fellowships (DGE 1762114 to I.K. and R.C.B.) from the National Science Foundation; Maximizing Investigators' Research Awards (R35GM138036 to C.A.D. and R35GM143081 to J.L.R.), research grants (R01CA289291 to C.A.D., R21CA283686 to C.A.D.), and an Interdisciplinary Training Grant (T32CA080416 to I.K.) from the National Institutes of Health. M.C.R. and work conducted in the Institute for Stem Cell and Regenerative Medicine (ISCRM) Genomics Core were supported by a generous gift from the John H. Tietze Foundation. The authors also acknowledge ISCRM (research scholarship to R.C.B.), the Mary Gates Endowment for Students (research scholarship to E.C.G.), and the Louis Stokes Alliance for Minority Participation (LSAMP) Program (research scholarship to K.R.V). The authors would additionally like to acknowledge Dr. Micah Glaz at the UW Molecular Analysis Facility for assisting with AFM method development, Dale Whittington and Dr. J. Scott Edgar (in memoriam) for assisting with LCMS, Dr. Dennis Wang at the UW Mitochondria and Metabolism Center for insightful discussion regarding metabolic assays, and Xinting Li for peptide synthesis help.

## Conflict of Interest

The authors declare no conflict of interest.

## Author Contributions

I.K., E.C.G., R.C.B., and C.A.D. conceived and designed the experiments. I.K., E.C.G., K.R.V., and R.C.B. executed the synthesis of material precursors, protein expression, and mass spectrometry. K.R.V. conducted photorheology experiments. I.K. conducted AFM, fluorescent release, and encapsulated cell culture experiments. E.C.G. carried out and analyzed cellular patterning experiments. S.Y. conducted multiphoton patterning and imaging. I.K. and J.W.H. designed and created the hMSC TEAD-reporter line. I.K., M.C.R., and J.W.H. conducted RNAseq library prep, sequencing, and analysis of data. I.K. and J.C.B conducted the hMSC differentiation assay and metabolic assays. I.K. and C.A.D. wrote the manuscript. I.K. and C.A.D. funded the experiments. C.A.D. provided mentorship and lab space.

## Data Availability Statement

The data that support the findings of this study are available from the corresponding author upon reasonable request.

## Keywords

bioorthogonal, hydrogels, interpenetrating polymer networks, mechanomemory, sortase, stimuli-responsive

Received: April 4, 2024
Revised: August 6, 2024

---

[1] T. Rozario, D. W. DeSimone, *Develop. Biol.* **2010**, *341*, 126.
[2] T. R. Cox, J. T. Erler, *Dis. Models Mech.* **2011**, *4*, 165.
[3] C. Bonnans, J. Chou, Z. Werb, *Nat. Rev. Mol. Cell Biol.* **2014**, *15*, 786.
[4] C. C. Dufort, M. J. Paszek, V. M. Weaver, *Nat. Rev. Mol. Cell Biol.* **2011**, *12*, 308.
[5] C. F. Guimarães, L. Gasperini, A. P. Marques, R. L. Reis, *Nat. Rev. Mater.* **2020**, *5*, 351.
[6] M. Jang, J. An, S. W. Oh, J. Y. Lim, J. Kim, J. K. Choi, J. H. Cheong, P. Kim, *Nat. Biomed. Eng.* **2021**, *5*, 114.
[7] S. Dupont, *Exp. Cell Res.* **2016**, *343*, 42.
[8] S. Dupont, L. Morsut, M. Aragona, E. Enzo, S. Giulitti, M. Cordenonsi, F. Zanconato, J. L. Digabel, M. Forcato, S. Bicciato, N. Elvassore, S. Piccolo, *Nature* **2011**, *474*, 179.
[9] K. M. Herum, J. Choppe, A. Kumar, A. J. Engler, A. D. McCulloch, *Mol. Biol. Cell* **2017**, *28*, 1871.
[10] K. R. Levental, H. Yu, L. Kass, J. N. Lakins, M. Egeblad, J. T. Erler, S. F. T. Fong, K. Csiszar, A. Giaccia, W. Weninger, M. Yamauchi, D. L. Gasser, V. M. Weaver, *Cell* **2009**, *139*, 891.
[11] B. Peltanova, M. Raudenska, M. Masarik, *Molecular Cancer* **2019**, *18*, 63.
[12] E. A. Aisenbrey, W. L. Murphy, *Nat. Rev. Mater.* **2020**, *5*, 539.
[13] K. A. Günay, T. L. Ceccato, J. S. Silver, K. L. Bannister, O. J. Bednarski, L. A. Leinwand, K. S. Anseth, *Angewandte Chemie – International Edition* **2019**, *58*, 9912.
[14] M. Guvendiren, J. A. Burdick, *Nat. Commun.* **2012**, *3*, 792.
[15] J. S. Silver, K. A. Günay, A. A. Cutler, T. O. Vogler, T. E. Brown, B. T. Pawlikowski, O. J. Bednarski, K. L. Bannister, C. J. Rogowski, A. G. Mckay, F. W. DelRio, B. B. Olwin, K. S. Anseth, *Sci. Adv.* **2021**, *7*, eabe4501.
[16] B. Timmons, M. Akins, M. Mahendroo, *Trends Endocrinol. Metab.* **2010**, *21*, 353.
[17] Y. Shen, X. Wang, J. Lu, M. Salfenmoser, N. M. Wirsik, N. Schleussner, A. Imle, A. F. Valls, P. Radhakrishnan, J. Liang, G. Wang, T. Muley, M. Schneider, C. R. de Almodovar, A. Diz-Muñoz, T. Schmidt, *Cancer Cell* **2020**, *37*, 800.
[18] E. Cambria, M. F. Coughlin, M. A. Floryan, G. S. Offeddu, S. E. Shelton, R. D. Kamm, *Nat. Rev. Cancer* **2024**, *24*, 216.
[19] A. M. Kloxin, A. M. Kasko, C. N. Salinas, K. S. Anseth, *Science* **2009**, *324*, 59.
[20] C. A. DeForest, K. S. Anseth, *Nat. Chem.* **2011**, *3*, 925.
[21] A. M. Rosales, S. L. Vega, F. W. DelRio, J. A. Burdick, K. S. Anseth, *Angew. Chem., Int. Ed.* **2017**, *56*, 12132.
[22] A. R. Killaars, J. C. Grim, C. J. Walker, E. A. Hushka, T. E. Brown, K. S. Anseth, *Adv. Sci.* **2019**, *6*, 1801483.
[23] C. J. Walker, C. Crocini, D. Ramirez, A. R. Killaars, J. C. Grim, B. A. Aguado, K. Clark, M. A. Allen, R. D. Dowell, L. A. Leinwand, K. S. Anseth, *Nat. Biomed. Eng.* **2021**, *5*, 1485.
[24] L. Liu, J. A. Shadish, C. K. Arakawa, K. Shi, J. Davis, C. A. DeForest, *Adv. Biosyst.* **2018**, *2*, 1800240.
[25] M. Hörner, K. Raute, B. Hummel, J. Madl, G. Creusen, O. S. Thomas, E. H. Christen, N. Hotz, R. J. Gübeli, R. Engesser, B. Rebmann, J. Lauer, B. Rolauffs, J. Timmer, W. W. A. Schamel, J. Pruszak, W. Römer, M. D. Zurbriggen, C. Friedrich, A. Walther, S. Minguet, R. Sawarkar, W. Weber, *Adv. Mater.* **2019**, *31*, 1806727.
[26] J. V. Accardo, J. A. Kalow, *Chem. Sci.* **2018**, *9*, 5987.
[27] F. X. Jiang, B. Yurke, B. L. Firestein, N. A. Langrana, *Ann. Biomed. Eng.* **2008**, *36*, 1565.
[28] S. Rammensee, M. S. Kang, K. Georgiou, S. Kumar, D. V. Schaffer, *Stem Cells* **2017**, *35*, 497.
[29] A. Buchberger, H. Saini, K. R. Eliato, A. Zare, R. Merkley, Y. Xu, J. Bernal, R. Ros, M. Nikkhah, N. Stephanopoulos, *ChemBioChem* **2021**, *22*, 1755.
[30] O. Jeon, T. H. Kim, E. Alsberg, *Acta Biomater.* **2021**, *136*, 88.
[31] Y. Shou, X. Y. Teo, X. Li, L. Zhicheng, L. Liu, X. Sun, W. Jonhson, J. Ding, C. T. Lim, A. Tay, *ACS Nano* **2023**, *17*, 2851.
[32] J. Valdez, C. D. Cook, C. C. Ahrens, A. J. Wang, A. Brown, M. Kumar, L. Stockdale, D. Rothenberg, K. Renggli, E. Gordon, D. Lauffenburger, F. White, L. Griffith, *Biomaterials* **2017**, *130*, 90.
[33] R. C. Bretherton, A. J. Haack, I. Kopyeva, F. Rahman, J. D. Kern, D. Bugg, A. B. Theberge, J. Davis, C. A. DeForest, *Adv. Mater.* **2023**, *35*, 2209904.
[34] M. R. Arkenberg, D. M. Moore, C. C. Lin, *Acta Biomater.* **2019**, *83*, 83.
[35] B. M. Dorr, H. O. Ham, C. An, E. L. Chaikof, D. R. Liu, *Proc. Natl. Acad. Sci. USA* **2014**, *111*, 13343.
[36] B. D. Fairbanks, M. P. Schwartz, A. E. Halevi, C. R. Nuttelman, C. N. Bowman, K. S. Anseth, *Adv. Mater.* **2009**, *21*, 5005.
[37] C. A. DeForest, D. A. Tirrell, *Nat. Mater.* **2015**, *14*, 523.
[38] C. A. DeForest, K. S. Anseth, *Angewandte Chemie – International Edition* **2012**, *51*, 1816.
[39] G. Liu, C. Zhou, W. L. Teo, C. Qian, Y. Zhao, *Angew Chem Int Ed* **2019**, *58*, 9366.
[40] S. Sharma, N. Monteleone, I. Kopyeva, S. J. Bryant, *J. Appl. Polym. Sci.* **2021**, *138*, e50786.
[41] B. A. Badeau, M. P. Comerford, C. K. Arakawa, J. A. Shadish, C. A. DeForest, *Nature Chem* **2018**, *10*, 251.
[42] M. D. A. Norman, S. A. Ferreira, G. M. Jowett, L. Bozec, E. Gentleman, *Nat. Protoc.* **2021**, *16*, 2418.
[43] I. Batalov, J. R. Filteau, R. M. Francis, G. Jaindl, L. Orr, T. L. Rapp, S. Yang, J. A. Filteau, W. Xie, R. C. Bretherton, A. K. Glaser, J. T. C. Liu, K. R. Stevens, C. A. DeForest, *bioRxiv* **2024**, https://doi.org/10.1101/2024.01.31.578280.
[44] D. R. Stirling, M. J. Swain-Bowden, A. M. Lucas, A. E. Carpenter, B. A. Cimini, A. Goodman, *BMC Bioinformatics* **2021**, *22*, 433.
[45] A. Dobin, C. A. Davis, F. Schlesinger, J. Drenkow, C. Zaleski, S. Jha, P. Batut, M. Chaisson, T. R. Gingeras, *Bioinformatics* **2013**, *29*, 15.
[46] M. I. Love, W. Huber, S. Anders, *Genome Biol.* **2014**, *15*, 550.
[47] A. Liberzon, A. Subramanian, R. Pinchback, H. Thorvaldsdóttir, P. Tamayo, J. P. Mesirov, *Bioinformatics* **2011**, *27*, 1739.
[48] Y. Li, M. D. Hoffman, D. S. W. Benoit, *Biomaterials* **2021**, *268*, 120535.
[49] M. Wang, W. Li, J. Hao, A. Gonzales, Z. Zhao, R. S. Flores, X. Kuang, X. Mu, T. Ching, G. Tang, Z. Luo, C. E. Garciamendez-Mijares, J. K. Sahoo, M. F. Wells, G. Niu, P. Agrawal, A. Quiñones-Hinojosa, K. Eggan, Y. S. Zhang, *Nat. Commun.* **2022**, *13*, 3317.
[50] K. L. Wiley, B. P. Sutherland, B. A. Ogunnaike, A. M. Kloxin, *Adv. Healthcare Mater.* **2022**, *11*, 2101947.
[51] H. M. Wyss, J. M. Henderson, F. J. Byfield, L. A. Bruggeman, Y. Ding, C. Huang, J. H. Suh, T. Franke, E. Mele, M. R. Pollak, J. H. Miner, P. A. Janmey, D. A. Weitz, R. T. Miller, *Am. J. Physiol. Cell Physiol.* **2011**, *300*, C397.

[52] S. Kawano, M. Kojima, Y. Higuchi, M. Sugimoto, K. Ikeda, N. Sakuyama, S. Takahashi, R. Hayashi, A. Ochiai, N. Saito, *Cancer Sci.* **2015**, *106*, 1232.
[53] A. Rubiano, D. Delitto, S. Han, M. Gerber, C. Galitz, J. Trevino, R. M. Thomas, S. J. Hughes, C. S. Simmons, *Acta Biomater.* **2018**, *67*, 331.
[54] C. F. Guimarães, L. Gasperini, A. P. Marques, R. L. Reis, *Nat. Rev. Mater.* **2020**, *5*, 351.
[55] N. Broguiere, F. A. Formica, G. Barreto, M. Zenobi-Wong, *Acta Biomater.* **2018**, *77*, 182.
[56] C. R. Below, J. Kelly, A. Brown, J. D. Humphries, C. Hutton, J. Xu, B. Y. Lee, C. Cintas, X. Zhang, V. Hernandez-Gordillo, L. Stockdale, M. A. Goldsworthy, J. Geraghty, L. Foster, D. A. O'Reilly, B. Schedding, J. Askari, J. Burns, N. Hodson, D. L. Smith, C. Lally, G. Ashton, D. Knight, A. Mironov, A. Banyard, J. A. Eble, J. P. Morton, M. J. Humphries, L. G. Griffith, C. Jørgensen, *Nat. Mater.* **2022**, *21*, 110.
[57] H. Shin, B. D. Olsen, A. Khademhosseini, *Biomaterials* **2012**, *33*, 3143.
[58] E. Ežerskytė, M. Vengris, K. Gineitis, G. Merkininkaitė, B. Leber, R. Vargalis, P. Stiegler, P. Schemmer, S. Šakirzanovas, A. Kielaitė-Gulla, K. Strupas, L. Jonušauskas, *Opt. Mater. Express, OME* **2022**, *12*, 2550.
[59] W. Zhang, P. Soman, K. Meggs, X. Qu, S. Chen, *Adv. Funct. Mater.* **2013**, *23*, 1202666.
[60] X. H. Qin, X. Wang, M. Rottmar, B. J. Nelson, K. Maniura-Weber, *Adv. Mater.* **2018**, *30*, 1705564.
[61] M. Colasurdo, E. B. Nieves, M. A. Fernández-Yagüe, C. Franck, A. J. García, *Biomaterials* **2022**, *288*, 121710.
[62] S. Khetan, M. Guvendiren, W. R. Legant, D. M. Cohen, C. S. Chen, J. A. Burdick, *Nature Mater* **2013**, *12*, 458.
[63] R. Subramani, A. Izquierdo-Alvarez, P. Bhattacharya, M. Meerts, P. Moldenaers, H. Ramon, H. Van Oosterwyck, *Front. Mater.* **2020**, *7*, 212.
[64] H. Long, B. E. Vos, T. Betz, B. M. Baker, B. Trappmann, *Adv. Sci.* **2022**, *9*, 2105325.
[65] T. Kaufman, E. Nitzan, N. Firestein, M. B. Ginzberg, S. Iyengar, N. Patel, R. Ben-Hamo, Z. Porat, J. Hunter, A. Hilfinger, V. Rotter, R. Kafri, R. Straussman, *Nat. Commun.* **2022**, *13*, 2725.
[66] K. C. Lin, H. W. Park, K. L. Guan, *Trends Biochem. Sci.* **2017**, *42*, 862.
[67] M. Aragona, T. Panciera, A. Manfrin, S. Giulitti, F. Michielin, N. Elvassore, S. Dupont, S. Piccolo, *Cell* **2013**, *154*, 1047.
[68] J. M. Franklin, R. P. Ghosh, Q. Shi, M. P. Reddick, J. T. Liphardt, *Nat. Commun.* **2020**, *11*, 4581.
[69] S. R. Caliari, S. L. Vega, M. Kwon, E. M. Soulas, J. A. Burdick, *Biomaterials* **2016**, *103*, 314.
[70] G. Brusatin, T. Panciera, A. Gandin, A. Citron, S. Piccolo, *Nature Mater* **2018**, *17*, 1063.
[71] C. Yang, M. W. Tibbitt, L. Basta, K. S. Anseth, *Nat. Mater.* **2014**, *13*, 645.
[72] E. Prouvé, M. Rémy, C. Feuillie, M. Molinari, P. Chevallier, B. Drouin, G. Laroche, M. C. Durrieu, *Biomater. Sci.* **2022**, *10*, 4978.
[73] L. S. Wang, C. Du, J. E. Chung, M. Kurisawa, *Acta Biomater.* **2012**, *8*, 1826.
[74] N. N. Rahbari, D. Kedrin, J. Incio, H. Liu, W. W. Ho, H. T. Nia, C. M. Edrich, K. Jung, J. Daubriac, I. Chen, T. Heishi, J. D. Martin, Y. Huang, N. Maimon, C. Reissfelder, J. Weitz, Y. Boucher, J. W. Clark, A. J. Grodzinsky, D. G. Duda, R. K. Jain, D. Fukumura, *Sci. Transl. Med.* **2016**, *8*, 360ra135.
[75] J. L. Chitty, M. Yam, L. Perryman, A. L. Parker, J. N. Skhinas, Y. F. I. Setargew, E. T. Y. Mok, E. Tran, R. D. Grant, S. L. Latham, B. A. Pereira, S. C. Ritchie, K. J. Murphy, M. Trpceski, A. D. Findlay, P. Melenec, E. C. Filipe, A. Nadalini, S. Velayuthar, G. Major, K. Wyllie, M. Papanicolaou, S. Ratnaseelan, P. A. Phillips, G. Sharbeen, J. Youkhana, A. Russo, A. Blackwell, J. F. Hastings, M. C. Lucas, et al., *Nat Cancer* **2023**, *4*, 1326.
[76] R. B. van Breemen, Y. Li, *Exp. Opin. Drug Metabol. Toxicol.* **2005**, *1*, 175.
[77] R. Rapier, J. Huq, R. Vishnubhotla, M. Bulic, C. M. Perrault, V. Metlushko, M. Cho, R. T. S. Tay, S. C. Glover, *Cancer Cell Int.* **2010**, *10*, 24.
[78] P. Deptuła, D. Łysik, K. Pogoda, M. Cieśluk, A. Namiot, J. Mystkowska, G. Król, S. Głuszek, P. A. Janmey, R. Bucki, *ACS Biomater. Sci. Eng.* **2020**, *6*, 5620.
[79] P. Thomas, A. Pranatharthi, C. Ross, S. Srivastava, *J. Exp. Clin. Cancer Res.* **2019**, *38*, 328.
[80] M. Iiizumi, S. Bandyopadhyay, S. K. Pai, M. Watabe, S. Hirota, S. Hosobe, T. Tsukada, K. Miura, K. Saito, E. Furuta, W. Liu, F. Xing, H. Okuda, A. Kobayashi, K. Watabe, *Cancer Res.* **2008**, *68*, 7613.
[81] O. Korkina, Z. Dong, A. Marullo, G. Warshaw, M. Symons, R. Ruggieri, *J. Biol. Chem.* **2013**, *288*, 5364.
[82] B. Wang, H. Guo, H. Yu, Y. Chen, H. Xu, G. Zhao, *Frontiers in Oncology* **2021**, *11*, 642547.
[83] J. Baek, P. A. Lopez, S. Lee, T. S. Kim, S. Kumar, D. V. Schaffer, *Sci Adv*, *8*, eabm4646.
[84] J. Omerovic, E. M. R. Puggioni, S. Napoletano, V. Visco, R. Fraioli, L. Frati, A. Gulino, M. Alimandi, *Exp. Cell Res.* **2004**, *294*, 469.
[85] S. Basu, N. F. Totty, M. S. Irwin, M. Sudol, J. Downward, *Mol. Cell* **2003**, *11*, 11.
[86] A. Subramanian, P. Tamayo, V. K. Mootha, S. Mukherjee, B. L. Ebert, M. A. Gillette, A. Paulovich, S. L. Pomeroy, T. R. Golub, E. S. Lander, J. P. Mesirov, *Proc. Natl. Acad. Sci. USA* **2005**, *102*, 15545.
[87] M. Martini, M. C. De Santis, L. Braccini, F. Gulluni, E. Hirsch, *Ann. Med.* **2014**, *46*, 372.
[88] T. Asano, Y. Yao, J. Zhu, D. Li, J. L. Abbruzzese, S. A. G. Reddy, *Oncogene* **2004**, *23*, 8571.
[89] J. Zhu, J. Blenis, J. Yuan, *Proc Natl Acad Sci U S A* **2008**, *105*, 6584.
[90] C. Saygili Demir, A. Sabine, M. Gong, O. Dormond, T. V. Petrova, *J. Cell Biol.* **2023**, *222*, 202207049.
[91] K. Satoh, S. Yachida, M. Sugimoto, M. Oshima, T. Nakagawa, S. Akamoto, S. Tabata, K. Saitoh, K. Kato, S. Sato, K. Igarashi, Y. Aizawa, R. Kajino-Sakamoto, Y. Kojima, T. Fujishita, A. Enomoto, A. Hirayama, T. Ishikawa, M. M. Taketo, Y. Kushida, R. Haba, K. Okano, M. Tomita, Y. Suzuki, S. Fukuda, M. Aoki, T. Soga, *Proc. Natl. Acad. Sci. USA* **2017**, *114*, E7697.
[92] N. Kugimiya, A. Nishimoto, T. Hosoyama, K. Ueno, T. Enoki, T. S. Li, K. Hamano, *J. Cell. Mol. Med.* **2015**, *19*, 1569.
[93] H. D. Nguyen, C. C. Lin, *Acta Biomater.* **2024**, *177*, 203.
[94] H. Q. Ju, J. F. Lin, T. Tian, D. Xie, R. H. Xu, *Sig Transduct Target Ther* **2020**, *5*, 231.
[95] G. Colombo, E. L. M. Gelardi, F. C. Balestrero, M. Moro, C. Travelli, A. A. Genazzani, *Front. Pharmacol.* **2021**, *12*, 758320.
[96] M. Al-Masri, K. Paliotti, R. Tran, R. Halaoui, V. Lelarge, S. Chatterjee, L. T. Wang, C. Moraes, L. McCaffrey, *Commun Biol* **2021**, *4*, 371.
[97] P. Lu, K. Takai, V. M. Weaver, Z. Werb, *Cold Spring Harb Perspect Biol* **2011**, *3*, a005058.
[98] P. Singh, C. Carraher, J. E. Schwarzbauer, *Annu. Rev. Cell Dev. Biol.* **2010**, *26*, 397.
[99] S. Ricard-Blum, *Cold Spring Harb Perspect Biol* **2011**, *3*, a004978.
[100] O. Chaudhuri, L. Gu, D. Klumpers, M. Darnell, S. A. Bencherif, J. C. Weaver, N. Huebsch, H. Lee, E. Lippens, G. N. Duda, D. J. Mooney, *Nature Mater* **2016**, *15*, 326.
[101] O. Chaudhuri, S. T. Koshy, C. Branco da Cunha, J. W. Shin, C. S. Verbeke, K. H. Allison, D. J. Mooney, *Nature Mater* **2014**, *13*, 970.
[102] G. Ciccone, O. Dobre, G. M. Gibson, J. M. Rey, C. Gonzalez-Garcia, M. Vassalli, M. Salmeron-Sanchez, M. Tassieri, *Adv. Healthcare Mater.* **2020**, *9*, 2000517.

[103] M. Walker, E. W. Pringle, G. Ciccone, L. Oliver-Cervelló, M. Tassieri, D. Gourdon, M. Cantini, *Adv. Healthcare Mater.* **2024**, *13*, 2302571.
[104] J. I. Bennett, M. O. Boit, N. E. Gregorio, F. Zhang, R. D. Kibler, J. W. Hoye, O. Prado, P. B. Rapp, C. E. Murry, K. R. Stevens, C. A. DeForest, *Adv. Sci.* **2024**, *11*, 2301708.
[105] S. I. Somo, K. Langert, C. Y. Yang, M. K. Vaicik, V. Ibarra, A. A. Appel, B. Akar, M. H. Cheng, E. M. Brey, *Acta Biomater.* **2018**, *65*, 53.
[106] R. M. Desai, S. T. Koshy, S. A. Hilderbrand, D. J. Mooney, N. S. Joshi, *Biomaterials* **2015**, *50*, 30.